



HAL
open science

Airborne Absolute Gravimetry With a Quantum Sensor, Comparison With Classical Technologies

Yannick Bidel, Nassim Zahzam, Alexandre Bresson, Cédric Blanchard, Alexis Bonnin, Jeanne Bernard, Malo Cadoret, Tim E Jensen, René Forsberg, C. Salaun, et al.

► **To cite this version:**

Yannick Bidel, Nassim Zahzam, Alexandre Bresson, Cédric Blanchard, Alexis Bonnin, et al.. Airborne Absolute Gravimetry With a Quantum Sensor, Comparison With Classical Technologies. Journal of Geophysical Research : Solid Earth, 2023, 128 (4), pp.e2022JB025921. 10.1029/2022JB025921 . hal-04618809

HAL Id: hal-04618809

<https://hal.science/hal-04618809>

Submitted on 20 Jun 2024

HAL is a multi-disciplinary open access archive for the deposit and dissemination of scientific research documents, whether they are published or not. The documents may come from teaching and research institutions in France or abroad, or from public or private research centers.

L'archive ouverte pluridisciplinaire **HAL**, est destinée au dépôt et à la diffusion de documents scientifiques de niveau recherche, publiés ou non, émanant des établissements d'enseignement et de recherche français ou étrangers, des laboratoires publics ou privés.



Distributed under a Creative Commons Attribution - NonCommercial - NoDerivatives 4.0 International License

JGR Solid Earth



RESEARCH ARTICLE

10.1029/2022JB025921

Airborne Absolute Gravimetry With a Quantum Sensor, Comparison With Classical Technologies

Y. Bidel¹ , N. Zahzam¹ , A. Bresson¹ , C. Blanchard¹, A. Bonnin¹, J. Bernard², M. Cadoret², T. E. Jensen³ , R. Forsberg³ , C. Salaun⁴, S. Lucas⁴, M. F. Lequentrec-Lalancette⁴, D. Rouxel⁴ , G. Gabalda⁵, L. Seoane⁵ , D. T. Vu⁵, S. Bruinsma⁵ , and S. Bonvalot⁵

¹DPHY, ONERA, Université Paris Saclay, Palaiseau, France, ²LCM-CNAM, La Plaine Saint-Denis, France, ³National Space Institute, Technical University of Denmark, Denmark, Denmark, ⁴Shom – French Hydrographic and Oceanographic Office, Brest, France, ⁵GET (CNRS, IRD, UPS, CNES) – University of Toulouse, Toulouse, France

Key Points:

- Unlike classical systems, a quantum gravimeter does not require calibrations or drift estimations during an airborne gravity campaign
- A quantum gravimeter has demonstrated similar precision than an Inertial Measurement Unit (IMU) gravimeter and significantly better precision than a spring gravimeter
- A quantum gravimeter has shown significantly better long-term stability than an IMU strapdown system even if its drift has been corrected

Correspondence to:

Y. Bidel,
yannick.bidel@onera.fr

Citation:

Bidel, Y., Zahzam, N., Bresson, A., Blanchard, C., Bonnin, A., Bernard, J., et al. (2023). Airborne absolute gravimetry with a quantum sensor, comparison with classical technologies. *Journal of Geophysical Research: Solid Earth*, 128, e2022JB025921. <https://doi.org/10.1029/2022JB025921>

Received 14 OCT 2022
Accepted 26 MAR 2023

Author Contributions:

Conceptualization: Y. Bidel, N. Zahzam, A. Bresson, M. Cadoret, T. E. Jensen, R. Forsberg, M. F. Lequentrec-Lalancette, D. Rouxel, S. Bonvalot

Formal analysis: Y. Bidel, A. Bonnin, T. E. Jensen, R. Forsberg, D. Rouxel, D. T. Vu, S. Bonvalot

Funding acquisition: A. Bresson, R. Forsberg, M. F. Lequentrec-Lalancette, D. Rouxel, S. Bruinsma, S. Bonvalot

Investigation: Y. Bidel, N. Zahzam, A. Bresson, C. Blanchard, J. Bernard, M. Cadoret, T. E. Jensen, R. Forsberg, C. Salaun, S. Lucas, M. F. Lequentrec-Lalancette, D. Rouxel, G. Gabalda, L. Seoane, S. Bonvalot

© 2023. The Authors.

This is an open access article under the terms of the [Creative Commons Attribution-NonCommercial-NoDerivs License](https://creativecommons.org/licenses/by/4.0/), which permits use and distribution in any medium, provided the original work is properly cited, the use is non-commercial and no modifications or adaptations are made.

Abstract We report an airborne gravity survey with an absolute gravimeter based on atom interferometry and two relative gravimeters: a classical LaCoste&Romberg (L&R) and a novel iMAR strapdown Inertial Measurement Unit. We estimated measurement errors for the quantum gravimeter ranging from 0.6 to 1.3 mGal depending on the flight conditions and the filtering used. Similar measurement errors are obtained with iMAR strapdown gravimeter, but the long-term stability is five times worse. The traditional L&R platform gravimeter shows larger measurement errors (3–4 mGal). Airborne measurements have been compared to marine, land, and altimetry-derived gravity data. We obtain a good agreement for the quantum gravimeter with standard deviations and means on differences below or equal to 2 mGal. This study confirms the potential of quantum technology for absolute airborne gravimetry, which is particularly interesting for mapping shallow water or mountainous areas and for linking ground and satellite measurements with homogeneous absolute referencing.

Plain Language Summary Quantum technology offers a new kind of sensor for airborne gravimetry. Contrary to classical technologies which can only measure variation of gravity from an aircraft, a quantum gravimeter provides directly an absolute measurement of gravity eliminating the necessity of calibrations and drift estimations. We report here an airborne survey with a quantum gravimeter and two classical gravimeters. We demonstrated that the quantum gravimeter reaches the same precision as the best classical gravimeter. The gravity measurements have also been validated with models derived from land and marine gravity measurements and satellite altimetry.

1. Introduction

A new technology of gravimetry based on atom interferometry (Berman, 1997) is emerging. It is particularly promising because it confers at the same time absolute measurements, long-term stability, high sensitivity, and robustness. No classical instruments include all these advantages. Indeed, quantum gravimeters can have the same accuracy as falling corner cube gravity instruments (Karcher et al., 2018). Like superconducting gravimeters, it is used to continuously monitor gravity with high long-term stability (Freier et al., 2016; Ménoiret et al., 2018). It has also been demonstrated that such technology could be implemented on moving vehicles like spring gravimeters or forced balanced accelerometers (Bidel et al., 2018, 2020; Huang et al., 2022). Atom interferometry technology is finally also studied for the next generation of sensor for space gravimetry (Lévêque et al., 2021; Reguzzoni et al., 2021; Trimeche et al., 2019; Zahzam et al., 2022).

In this paper, we focus on airborne gravimetry (Forsberg & Olesen, 2010), which is a powerful tool for regional gravity mapping. It allows higher spatial resolution than space gravimetry (Kvas et al., 2019; Pail et al., 2011; Sandwell et al., 2014) and can cover areas that are difficult to map with ground gravimeters like mountains, glaciers, or deserts. Airborne gravimetry is also especially interesting in the coastal areas where satellite altimetry is not precise. In this context, quantum gravimeters are particularly interesting for airborne surveys because it is one of the technologies that provide absolute gravity measurements. Other technologies as spring-type gravimeters provide only variation of gravity and those based on force-balanced accelerometers suffer from important bias and instrumental drift that make calibration and data processing more difficult than those for quantum gravimeters. Quantum gravimetry could thus make airborne surveys faster, cheaper, and more precise since there

Methodology: Y. Bidel, N. Zahzam, A. Bresson, T. E. Jensen, R. Forsberg, D. Rouxel, D. T. Vu, S. Bonvalot
Project Administration: A. Bresson, R. Forsberg, D. Rouxel, S. Bonvalot
Resources: Y. Bidel, N. Zahzam, A. Bresson, C. Blanchard, T. E. Jensen, R. Forsberg, C. Salaun, S. Lucas, M. F. Lequentrec-Lalancette, D. Rouxel, G. Gabalda, L. Seoane, S. Bonvalot
Supervision: A. Bresson, R. Forsberg, M. F. Lequentrec-Lalancette, D. Rouxel, S. Bonvalot
Validation: Y. Bidel, T. E. Jensen, R. Forsberg, D. Rouxel, D. T. Vu, S. Bonvalot
Visualization: Y. Bidel, D. T. Vu
Writing – original draft: Y. Bidel, T. E. Jensen, D. T. Vu
Writing – review & editing: Y. Bidel, N. Zahzam, A. Bresson, A. Bonnin, T. E. Jensen, R. Forsberg, D. Rouxel, D. T. Vu, S. Bonvalot

is no need for calibration and drift estimations. The technology might also be very useful for correcting historical land and marine gravity data, which are often biased.

Within the last few years, a dynamic quantum sensor developed by the French aerospace lab ONERA for the hydrographic and oceanographic marine office (Shom) and the French Defence Agency (DGA) has been successfully tested in field conditions. Results derived from shipborne surveys and comparisons with other conventional marine gravity meter (Bodensee KSS32) and with satellite altimetry data confirmed the ability of quantum technologies for measuring absolute gravity in dynamic surveys with unprecedented robustness and accuracy below 1 mGal (Bidel et al., 2018). Initially designed for marine surveys, the same quantum sensor (hereafter called GIRAFE) has been also tested during an airborne survey. This first experiment also confirmed the capabilities of such quantum technologies for measuring absolute gravity from an aircraft with precision measurements ranging from 1.7 to 3.9 mGal (Bidel et al., 2020). Considering the promising perspectives derived from these results for future geophysical surveys, a dedicated airborne campaign has been proposed for assessing the potentialities and accuracy of airborne absolute gravimetry for surveying coastal, marine, and mountainous areas (Bonvalot et al., 2018). An improved version of the GIRAFE quantum gravimeter used in the previous campaign was used and compared with a LaCoste&Romberg (L&R) platform gravimeter and with an iMAR strapdown gravimeter. Here, we report the results from these airborne gravity surveys carried out in selected areas where data acquisition still remains challenging (land-sea transition and mountain range) and from a reference profile. Quantum gravity data measurements are compared with simultaneous measurements performed by other conventional instruments and with available information coming from satellite, marine, and terrestrial gravity measurements.

This article is organized as follows. In the first part, the quantum gravimeter and two mobile gravimetry systems are shortly described detailing the modification of the quantum gravimeter compared to the last campaign (Bidel et al., 2020). Then, in the second part, airborne data acquisitions are described and computed gravity disturbances are shown. Ground gravity measurements acquired during the campaign are also presented to check the accuracy and the long-term stability of GIRAFE gravimeter. In the third part, the errors of airborne measurements are estimated from repeated measurements at the same location. In the fourth part, gravity measured by the three instruments is inter-compared. Finally, in the last part, airborne gravity measurements are compared to models derived from land, marine gravity measurements, and satellite altimetry.

2. Dynamic Gravity Meters

2.1. GIRAFE Quantum Gravimeter

The quantum gravimeter (GIRAFE) used during this campaign is an improved version of the quantum gravimeter previously tested on a boat (Bidel et al., 2018) and aircraft (Bidel et al., 2020). Details of the principles and main characteristics of the instrument can be found in the abovementioned papers. A photograph of GIRAFE gravimeter deployed in the aircraft is shown in Figure 1. In this part, we will present a brief description of the gravimeter, emphasizing the improvements made compared to the previous airborne campaign (Bidel et al., 2020).

The gravimeter is composed of an absolute atom accelerometer, a gyro-stabilized platform that maintains the accelerometer aligned with the local gravity vector and systems which provide the lasers and microwaves needed to the atom sensor and perform data acquisition and processing.

The absolute accelerometer is based on the acceleration measurement of a free-falling gas of cold atoms by atom interferometry (Berman, 1997; Tino & Kasevich, 2014). The measurement sequence has three steps. First, a cloud of cold atoms (^{87}Rb) is prepared by laser cooling and trapping method (Metcalf & Van der Straten, 2007). Then, the free-falling atoms are submitted to three laser pulses which split, redirect and recombine the atom wave function. Finally, the signal of atom interference is recorded by fluorescence detection. The signal obtained is proportional to the cosine of the acceleration a :

$$P = P_m + \frac{C}{2} \cos\left(\frac{4\pi}{\lambda} \times a \times T^2\right) \quad (1)$$

In this expression, $\lambda = 780 \text{ nm}$ is the wavelength of the laser performing atom interferometry and T is the duration between the laser pulses which is equal to 20 ms in nominal condition or 10 ms in the presence of large variations of acceleration. Our sensor provides measurements at a repetition rate of 10 Hz. The atom accelerometer has the advantage to provide an absolute measurement of the acceleration, but it has measurement dead times during the

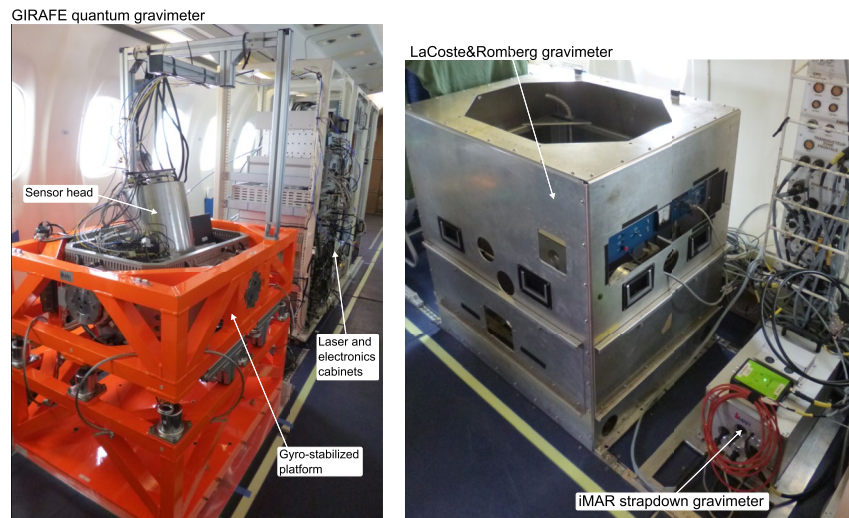


Figure 1. Photographs of the gravimeters deployed inside the ATR-42 aircraft from SAFIRE.

cold atom preparation and the detection. Moreover, many values of acceleration are possible for a given signal of the atom sensor due to the inversion of the cosine function. To overcome these limitations, the atom accelerometer is hybridized to a force-balanced accelerometer which fills the measurement dead times and lifts the ambiguity of the cosine function by providing an approximate value of the acceleration. On the other hand, the atom accelerometer estimates continuously the bias of the classical accelerometer.

In this improved version of the gravimeter, we modified the hybridization protocol by estimating continuously also the scale factor of the auxiliary force-balanced accelerometer in GIRAFE. The control loop for the correction of the scale factor is using an error signal equal to $\Delta a(a - g_0)$ where Δa is the acceleration difference measured between the classical and the atom accelerometer and $g_0 = 9.8 \text{ m s}^{-2}$ is the mean gravity. This improvement is particularly important during turbulent parts of a flight where there are large variations of acceleration. The horizontal lever arm between the measurement points of the atom and the classical accelerometer has been decreased. This horizontal lever arm is now 0.4 mm instead of 4.2 mm previously. With this improvement, we obtain a better agreement between the accelerations measured by the atom and the classical sensor in the presence of angular accelerations. We also synchronize the measurement sequence with a Pulse Per Second signal coming from the Global Navigation Satellite System (GNSS). This allows to have a perfect synchronization between the measurement of the gravimeter and GNSS navigation data and thus improving the correction of kinematic acceleration estimated by GNSS. Missing measurement points (Bidel et al., 2020) have now been almost completely eliminated. Finally, the laser system has been improved by using now an all-fiber laser system that is not subjected to possible misalignments. Indeed, in our laser system based on a frequency-doubled telecom fiber bench (Carraz et al., 2009), the free space frequency doubling in a bulk crystal has been replaced by a frequency doubling in a waveguide crystal (Lévêque et al., 2014).

In static conditions and for $T = 20 \text{ ms}$, the measurement sensitivity of the gravimeter is equal to $0.8 \text{ mGal/Hz}^{1/2}$ and the accuracy is equal to 0.17 mGal (Bidel et al., 2018).

2.2. Classical Gravimeters

Two conventional airborne gravimeters were additionally installed on board the aircraft. The first was an older L&R S-type gravimeter mounted on a two-axis damped platform (Valliant, 1992), the second a navigation-grade Inertial Measurement Unit (IMU) with temperature stabilization from iMAR Navigation, mounted in a strap-down configuration (Jensen et al., 2019). A photograph of these gravimeters deployed in the aircraft is shown in Figure 1. Both of these instruments are used to measure variations in the gravity field with respect to base readings performed on the ground before and after flight. The strapdown IMU system contains an internal GNSS receiver providing time-stamped observations synchronized with respect to GNSS navigation data. The L&R observations are time synchronized by deriving vertical accelerations from an external GNSS receiver and applying a constant time shift to optimize the correlation between both acceleration data streams.

3. Airborne Gravity Data Acquisition and Processing

3.1. Main Description and Objectives

The airborne gravity campaign took place in April–May 2019 across France, using an ATR-42 aircraft from SAFIRE (French facility for airborne research) located in Toulouse Franczal airport.

As mentioned above, the main objectives were (a) to assess the accuracy of the quantum GIRAFE instrument in comparison with other conventional gravity meters currently used for airborne gravimetry and (b) to evaluate the added value of such instrumentation for improving the gravity mapping of areas poorly covered by surface or satellite gravity measurements all such as land-sea transitions and mountainous regions. To fulfill these objectives, we first installed on board the aircraft two classical airborne gravimeters for performing simultaneous data acquisition with the quantum GIRAFE instrument. Second, two survey areas were selected on the western Atlantic shore over the Bay of Biscay, where both deep (up to $-2,000$ m) and shallow waters could be surveyed, and a southern area encompassing progressively the Pyrenees mountain range (heights up to $3,000$ m or more) and flat regions (heights from 150 to 200 m). In addition, a reference profile located off shore of Brittany and currently used by Shom for testing marine gravimeters has been repeated for assessing and comparing the accuracy of all embarked instruments. This reference line, also measured with GIRAFE instrument during the previous shipborne surveys (Bidel et al., 2018), will also enable to compare the performances of GIRAFE quantum meter in both airborne and shipborne surveying.

The flight lines for the three selected areas surveyed during spring 2019 are given in Figure 2 and Table 1. They include four gravity measurements flights (approximately 30 hr) acquired as follows. The first and second flights took place on 23 and 24 April and consisted of a survey over the Bay of Biscay to demonstrate the ability to map the land-sea transition. The first flight was dedicated to measure gravity along five North-South lines and the second flight was dedicated to measure gravity along six West-East lines. During these two flights, the altitude was $1,500$ m. The third flight took place on 25 April and consisted of five repeated measurements over the reference profile off shore of Brest at an altitude of 480 m. Finally, the fourth flight took place on 24 May over the Pyrenees for demonstrating the ability to map mountain areas. We measured gravity above Pyrenees along nine lines at an altitude of $4,400$ m.

The along-track plane velocity was around $v = 100$ m/s for all flights. The vertical accelerations experienced by the gravimeters during the four gravity measurement flights are given in Figure 2. During turbulent parts, vertical acceleration variations can reach 10 m/s² peak-peak, and during quiet parts, acceleration variations are below 1 m/s² peak-peak.

3.2. Ground Measurements

Throughout the airborne campaign from 19 April to 24 May, ground gravity measurements in the plane hangar and in the apron were performed by GIRAFE gravimeter installed in the aircraft. The results are given in Figure 3. The set scatter of absolute gravity values is 0.22 mGal peak-peak for measurements in the plane hangar and 0.64 mGal peak-peak for measurements in the plane apron. These set scatters agree with the estimated statistical uncertainty of the measurements confirming the long-term stability of the gravimeter even after the shocks, vibrations, and accelerations which occur during flight and after night electrical shutdown.

To provide an accurate ground reference gravity value for the airborne survey, absolute gravity measurements were also carried out during the campaign at both Toulouse-Franczal and Brest airports using A10 Micro-g LaCoste absolute gravity meters, A10 #014 and A10 #031, respectively (uncertainty 0.01 mGal). The absolute gravity values determined on ground within few tens of meters from the aircraft with the A10 instruments, were tied at the mean location of the instrument using CG-6 relative gravity meters. A first series of measurements was carried out in the hangar of Toulouse Franczal airport, where the aircraft was parked. A second series was done on the apron of Toulouse Franczal airport, where the aircraft was parked just before the takeoff. Finally, gravity measurements were done in Brest airport tarmac on the occasion of refueling for the flight off shore over the reference profile. The gravity values obtained by CG-6 and GIRAFE gravimeters are shown in Table 2. For Toulouse Franczal and Brest airport aprons, the measurements of GIRAFE gravimeter are in excellent agreement with the measurements of the calibrated CG-6 (≤ 0.1 mGal), while for Toulouse Franczal airport hangar, we obtain a difference of 0.3 – 0.4 mGal, larger than the estimated uncertainty which we could not explain.

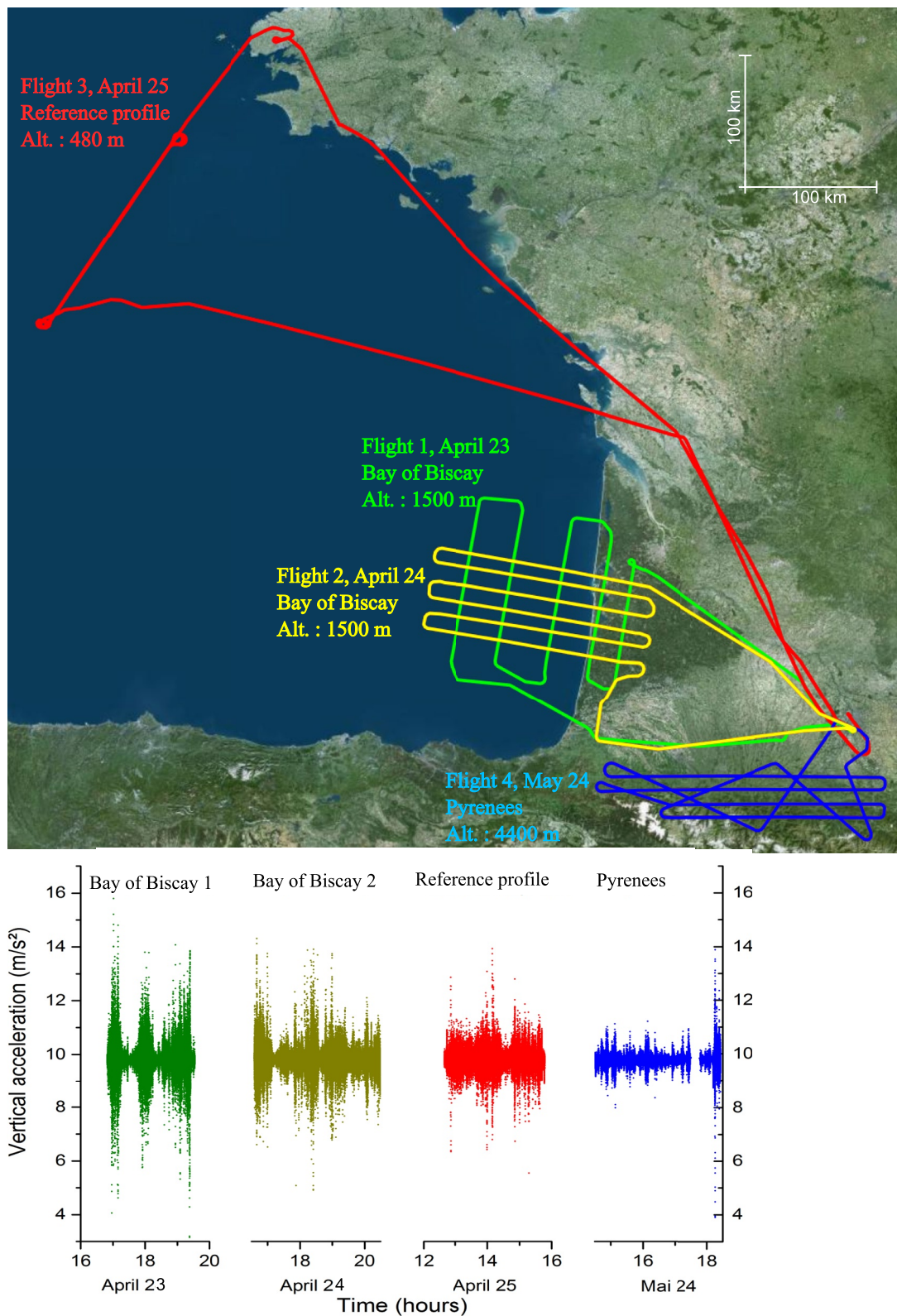


Figure 2. Top: Flight plan of the gravity campaign. Bottom: Vertical accelerations measured by the quantum gravimeter at a rate of 10 Hz during the flights.

Table 1
Overview of the Measurement Flights and Characteristics

Flight #	Date	Survey	Altitude	Descriptions
1	23 April 2019	Bay of Biscay	1,500 m	5 North-South lines
2	24 April 2019	Bay of Biscay	1,500 m	6 West-East lines
3	25 April 2019	Reference profile	480 m	5 repeated lines
4	24 May 2019	Pyrenees	4,400 m	9 lines

3.3. Computation of Gravity Disturbances

All data have been processed to compute the gravity disturbances. Detail of the data processing used to derive gravity disturbance from gravimeters measurements and GNSS data is described in Appendix A. The final maps of disturbances estimated from the three gravimeters along the flight lines at flight altitude are given in Figures 4 and 5 for Bay of Biscay and Pyrenees areas, respectively, in Figure 6 for the reference profile. Turns or lines with bad data acquisition for the different gravity meters used during surveys were removed. Note that laser frequency locking problems occurred on GIRAFE gravimeter on 24 May during Pyrenees flight prevented us to acquire data along certain lines. The gravity disturbance derived from the marine, land,

and altimetry gravity data projected on the flight lines is also given for reference. At a glance, we can see that GIRAFE and iMAR mostly show comparable acquisition lines, while the L&R meter led to less useable data acquisition. Gravity anomaly patterns and amplitudes revealed by all meters are close to the expected ones derived from marine, land, and altimetry data. The gravity disturbances obtained from the three gravity sensors along the flight lines are analyzed hereafter to estimate the measurement errors and the stability.

4. Estimation of the Precision of the Gravimeters From Repeated Measurements

4.1. Measurement Precision

The precision of the gravity measurements can be estimated by analyzing the differences between gravity measurements performed at the same location. For the reference profile, repeated measurements over the same line are compared and for the Bay of Biscay and Pyrenees, crossing point differences are analyzed (see Figure 7). Note that the cross-over analysis has not been done for L&R gravimeter in Biscay Bay because there are only two crossing points.

Assuming uncorrelated errors between measurements, the estimated error can be computed using the following expression:

$$\epsilon_{\delta g} = \frac{1}{\sqrt{2}} \sqrt{\frac{1}{N} \sum_{\substack{n, i, j \\ i > j}} (\delta g_i(r_n) - \delta g_j(r_n))^2} \quad (2)$$

where $\delta g_i(r_n)$ is the gravity disturbance measured at the position r_n at the i th pass and N is the number of elements in the sum.

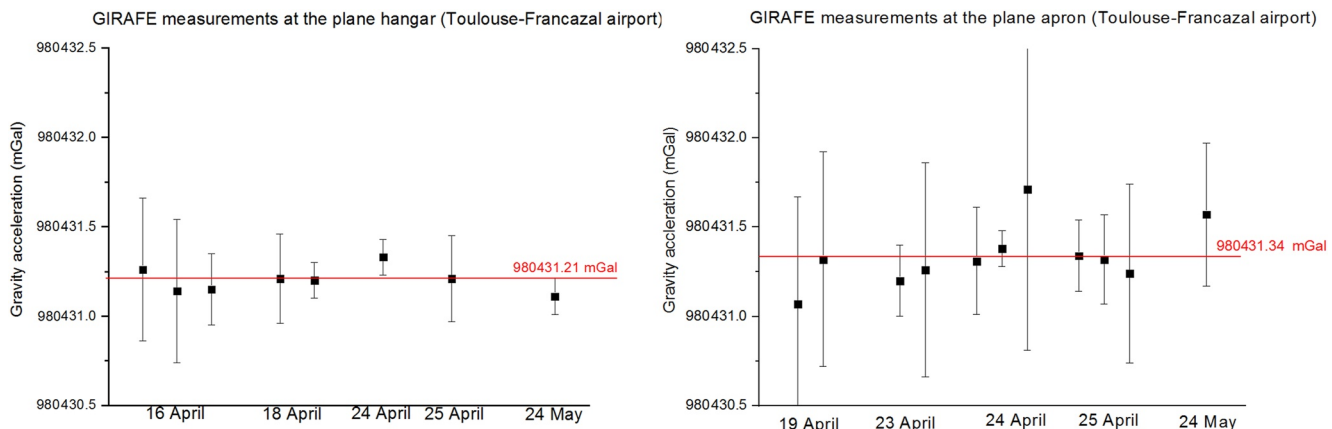


Figure 3. Ground gravity measurements with GIRAFE gravimeter installed in the aircraft. These measurements were done in Toulouse Francazal airport in the SAFIRE hangar (left) and on the apron (right). The error bars represent the statistical uncertainty of measurements and depend on the amplitude of the aircraft movement and on the duration of the measurements which are ranging from 8 to 60 min. The red line is the weighted average of the displayed gravity measurements.

Table 2
Gravity Ground Measurements

Location	Gravimeter	Gravity measurement (mGal)	Height (m)	Difference between GIRAFE and A10/CG-6 (height correction: 0.30 mGal/m) (mGal)
Toulouse Francazal airport hangar	GIRAFE on the ground	980,431.50 ± 0.17	1.03	0.36 ± 0.17
	GIRAFE in the aircraft	980,431.21 ± 0.18	2.1	0.39 ± 0.18
	A10/CG-6 on the ground	980,431.45 ± 0.01	0	
Toulouse Francazal airport apron	GIRAFE in the aircraft	980,431.34 ± 0.18	2.1	0.11 ± 0.18
	A10/CG-6 on the ground	980,431.86 ± 0.01	0	
Brest airport apron	GIRAFE in the aircraft	980,915.08 ± 0.30	2.1	0.06 ± 0.3
	A10/CG-6 on the ground	980,915.65 ± 0.01	0	

Note. Tidal corrections (Tamura, 1987) were applied to the A10/CG-6 and GIRAFE measurements. Intervals are given at 1 σ .

The influence of the cutoff frequency of the used Gaussian low pass filter in the GIRAFE gravimeter data processing has been studied (see A4). In the following, the filter will be characterized by its FWHM pulse response $\Delta\tau$. The spatial resolution of the measurements, that is, the FWHM response to an infinitely narrow gravity anomaly peak (Dirac delta function) is then equal to $v \times \Delta\tau$ with v the plane velocity. In Figure 8, we plot the estimated errors for the three surveys versus the FWHM pulse response $\Delta\tau$. For the three surveys, there is a value of $\Delta\tau$ which minimizes the error. However, the optimal $\Delta\tau$ is different for each survey. For small values of $\Delta\tau$, the estimated error is smaller for Pyrenees and reference profile than for Biscay bay. This could be explained by the fact that Biscay flights were the most turbulent leading to a larger measurement noise. For large values of $\Delta\tau$ the estimated error is smaller for the reference profile than Bay of Biscay and Pyrenees. This can be explained first by the fact that the measurement line on the reference profile is longer leading to less border effects, but also due to the

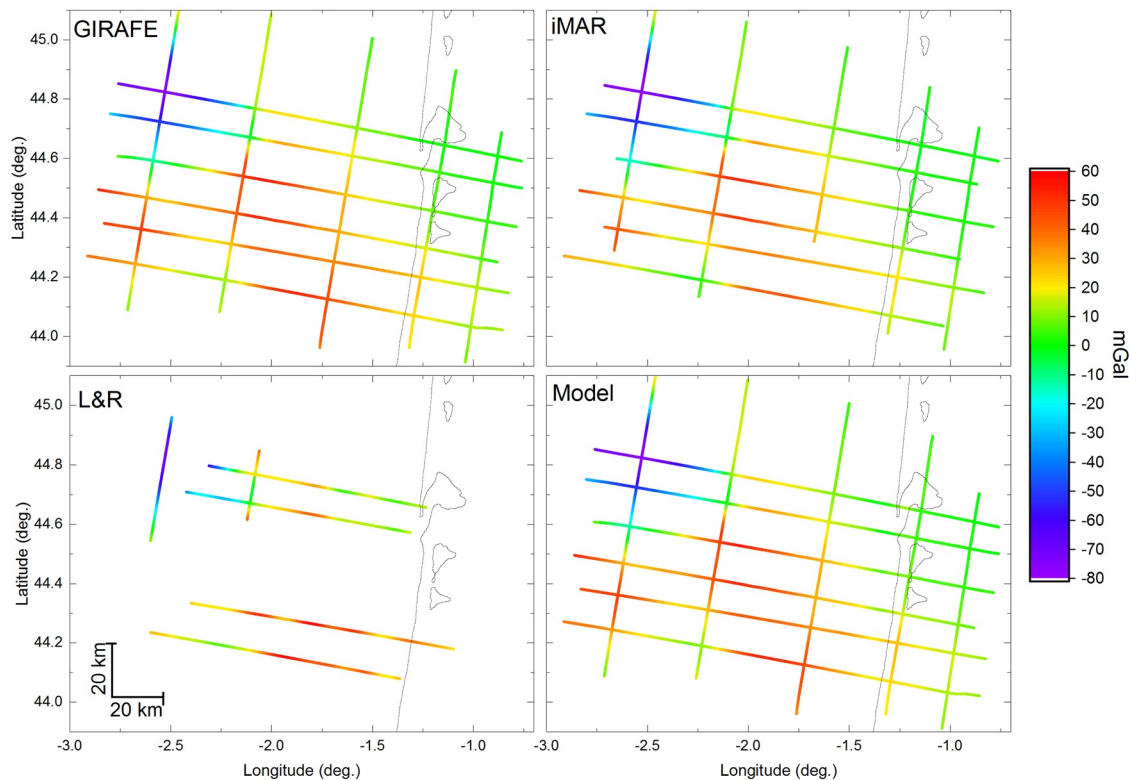


Figure 4. Gravity disturbance over Biscay Bay measured by the three gravimeters and model at the flight altitude derived from satellite altimetry and land gravimetry data (see Section 6). The filter used for GIRAFE data processing leads to a full-width-half-maximum spatial resolution of 7 km (see Section A4). The missing LaCoste&Romberg (L&R) data are due to excessive turbulence.

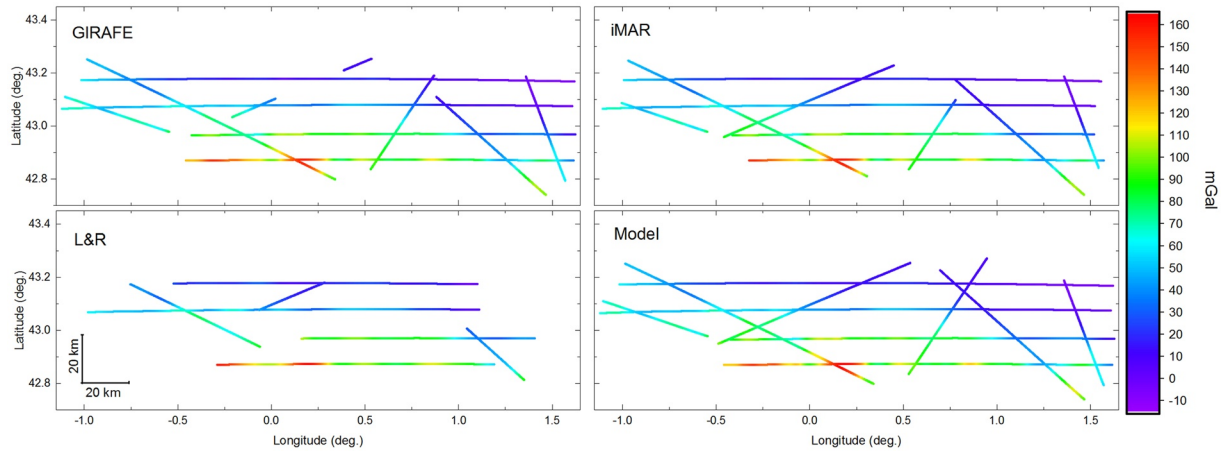


Figure 5. Gravity disturbance over Pyrenees measured by the three gravimeters and gravity models at the flight altitude (see Section 6). The filter used for GIRAFA data processing leads to a full-width-half-maximum spatial resolution of 4.5 km (see Section A4). The model values are from upward continued land gravity data in France and Spain.

differences in turbulence. Second, the error is estimated by comparing measurements acquired on the same line for the reference profile and on different lines for Biscay bay and Pyrenees. As the low pass filter makes a spatial filtering only on a 1D line, spatially unresolved gravity anomaly can lead to different gravity measurements if differently oriented measurement lines are used. This directional effect is especially important in the Pyrenees flights, where the local gravity variations are much higher, and more anisotropic, than in the marine flights.

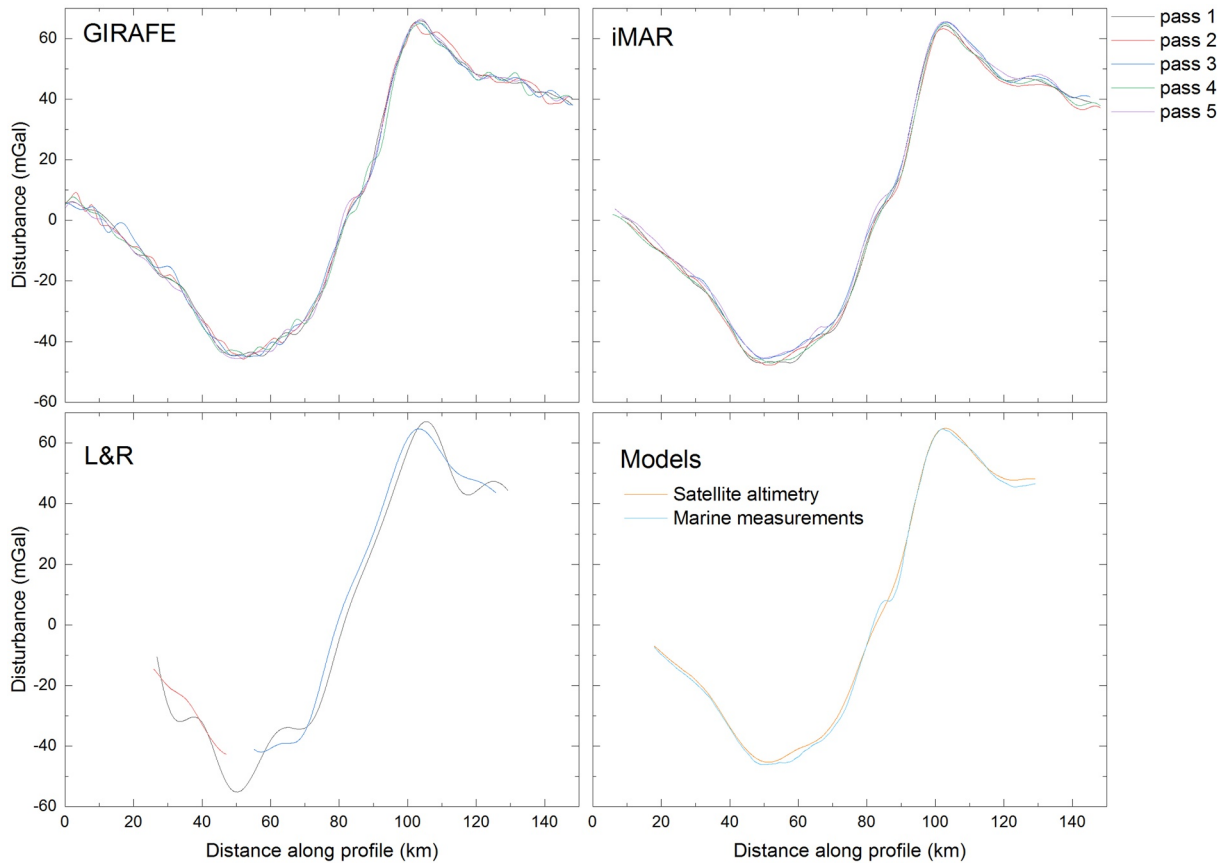


Figure 6. Gravity disturbance along the reference profile measured by the three gravimeters and gravity models at the flight altitude (see Section 6). The filter used for GIRAFA data processing leads to a full-width-half-maximum spatial resolution of 4.5 km (see Section A4).

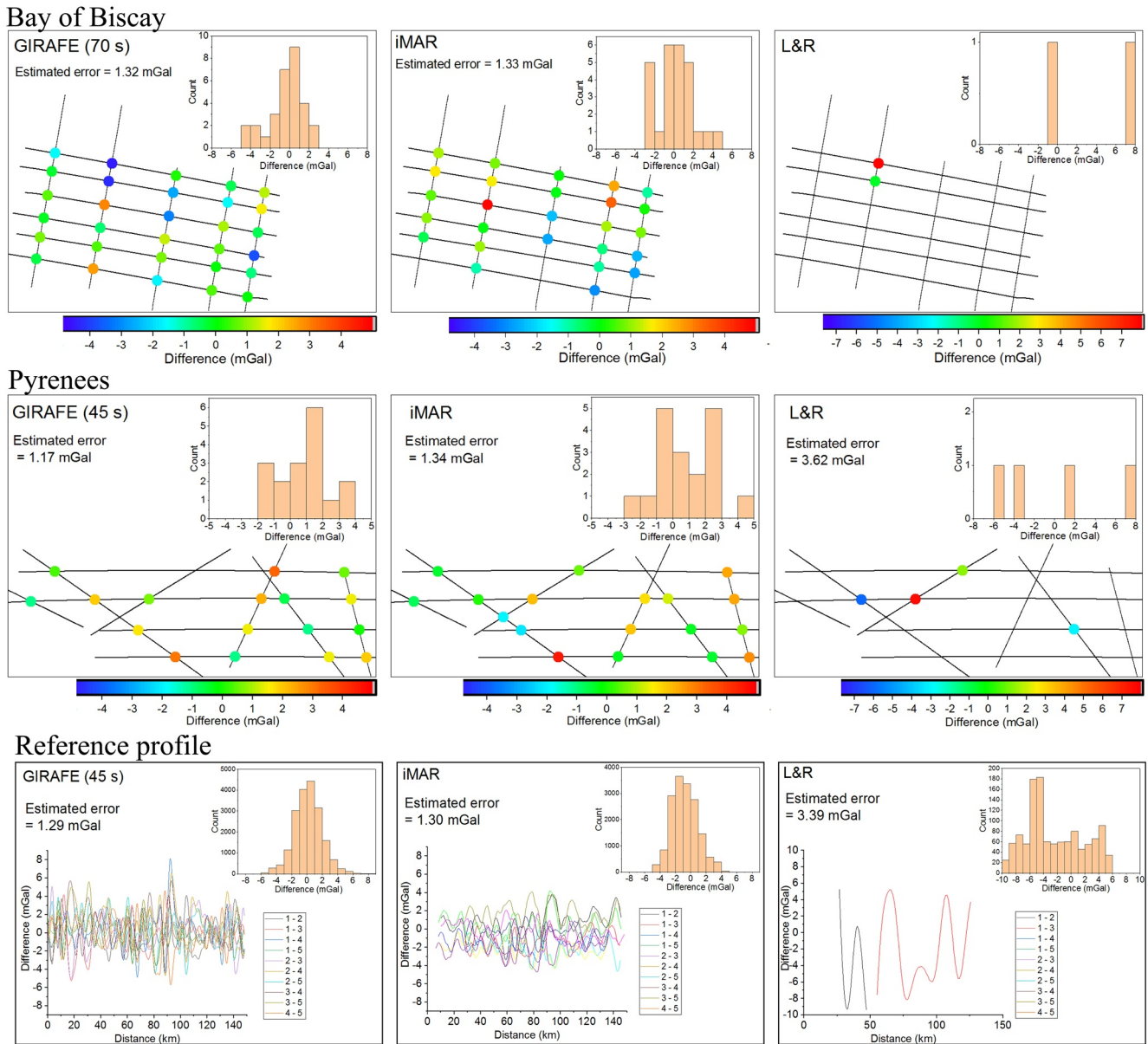


Figure 7. Crossing points analysis and repeated profile analysis. The first and second rows show the crossing point differences for Bay of Biscay and Pyrenees survey. The last row shows the differences between the five repeated lines over the reference profile. The curves labeled i - j represent the difference between the gravity measured at i th pass and j th pass. On each graph, the upper-right insert is the histogram of the differences showed on the graph. The FWHM pulse response $\Delta\tau$ of the filter used in GIRAPE data processing is 70 s for Bay of Biscay, 45 s for Pyrenees and reference profile.

In Table 3, the estimated errors for the three gravimeters and for each area are summarized. To have a meaningful comparison, the low pass filter used for GIRAPE data processing has been selected to minimize the RMS differences with iMAR measurements (see Section 5). If we assume that both gravimeters have the same noise level, this choice leads to the same spatial resolution.

GIRAPE and iMAR have approximately the same measurement errors ranging from 1.2 to 1.3 mGal. On the other side, L&R gravimeter has larger errors ranging from 3.4 to 3.6 mGal. Indeed, the L&R platform is quite sensitive to turbulence and dynamic flight conditions. A more quantitative analysis of the data has been performed in Appendix B. This analysis confirms that the precision of GIRAPE and iMAR are not significantly different, while L&R precision is significantly worse. For the reference profile and Pyrenees, we also found significant correlations in the measurement errors between iMAR and GIRAPE which may come from GNSS errors that impact the

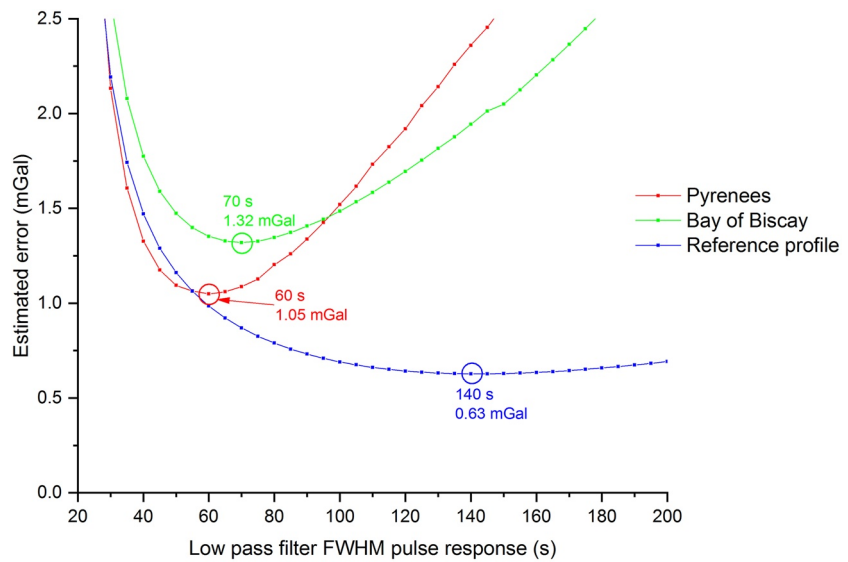


Figure 8. Estimated error on GIRAFE gravity measurements versus the full-width-half-maximum (FWHM) pulse response of the low pass filter $\Delta\tau$ used in the data processing.

estimation of gravity of both gravimeters. We observed also for reference profile, a significant difference in the mean value between iMAR and GIRAFE highlighting the drift of iMAR gravimeter.

4.2. Stability of Gravity Measurements

The stability of the gravity measurements during the flight is estimated by comparing the mean values of the gravity disturbance measured at each pass over the reference profile (see Figure 9). The standard deviation on the gravity mean values is clearly smaller for GIRAFE gravimeter (0.22 mGal) than for iMAR (1.05 mGal) and L&R (1.76 mGal). This confirms the advantage of GIRAFE gravimeters over traditional gravimeters even if these ones have been calibrated and the drift is compensated for.

5. Comparison of Gravity Disturbance Estimated by the Three Gravimeters

The gravity disturbance estimated from the measurements of the three gravimeters has been compared in Figures 10 and 11. GIRAFE, iMAR, and L&R all flew at the same time. For the reference profile, the gravity disturbance is averaged over five passes for GIRAFE and iMAR and over only two passes for L&R because due to excessive turbulence some L&R data were not useful.

We study here also the influence of the low pass filter used for GIRAFE data processing (see appendix A4). This low pass filter acts on the measurement noise and on the spatial resolution. We observe that a filter FWHM

pulse response $\Delta\tau$ minimizes the standard deviation of the difference between gravimeter measurements. For iMAR, the minimum is 45 s for Pyrenees and reference profile and 70 s for Bay of Biscay. For L&R, the minimum is 70 s for Pyrenees and reference profile and 100 s for Bay of Biscay. Those minimums result in a compromise between spatial resolution matching between gravity measurements and GIRAFE measurement noise minimizing. Neglecting GIRAFE measurement noise, the minimum corresponds to the point where the measurements of both gravimeters have the same spatial resolution.

The standard deviations on the differences for those minimums are summarized in Table 4. They are compared to the estimation obtained by summing quadratically each gravimeter error calculated from repeated measurements at the same location (see Table 3). For the reference profile, the error on

Table 3
Gravity Measurement Errors Estimated From Repeated Measurements (mGal)

	Bay of Biscay	Reference profile	Pyrenees
GIRAFE quantum gravimeter	1.32 ($\Delta\tau = 70$ s)	1.29 ($\Delta\tau = 45$ s)	1.17 ($\Delta\tau = 45$ s)
iMAR strapdown gravimeter	1.33	1.30	1.34
L&R platform gravimeter	Undetermined	3.39	3.62

Note. For L&R the gravity measurement errors are estimated after the Butterworth filtering described in Appendix A5.

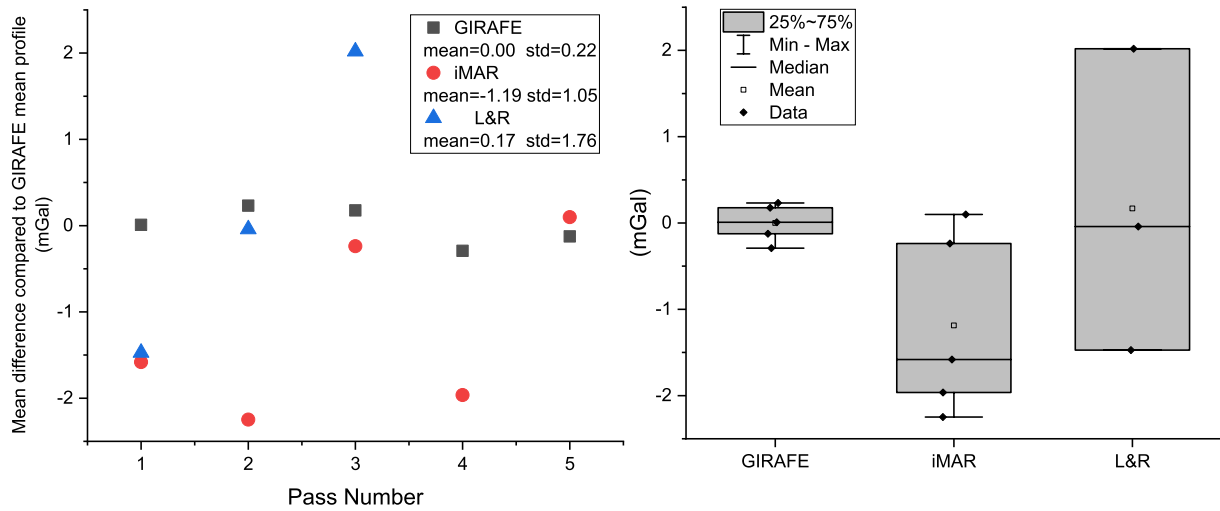


Figure 9. Stability of gravity measurements over the reference profile. Left: Mean values of the gravity disturbance measured at each pass over the reference profile. Right: Box plots of the mean values for each gravimeter.

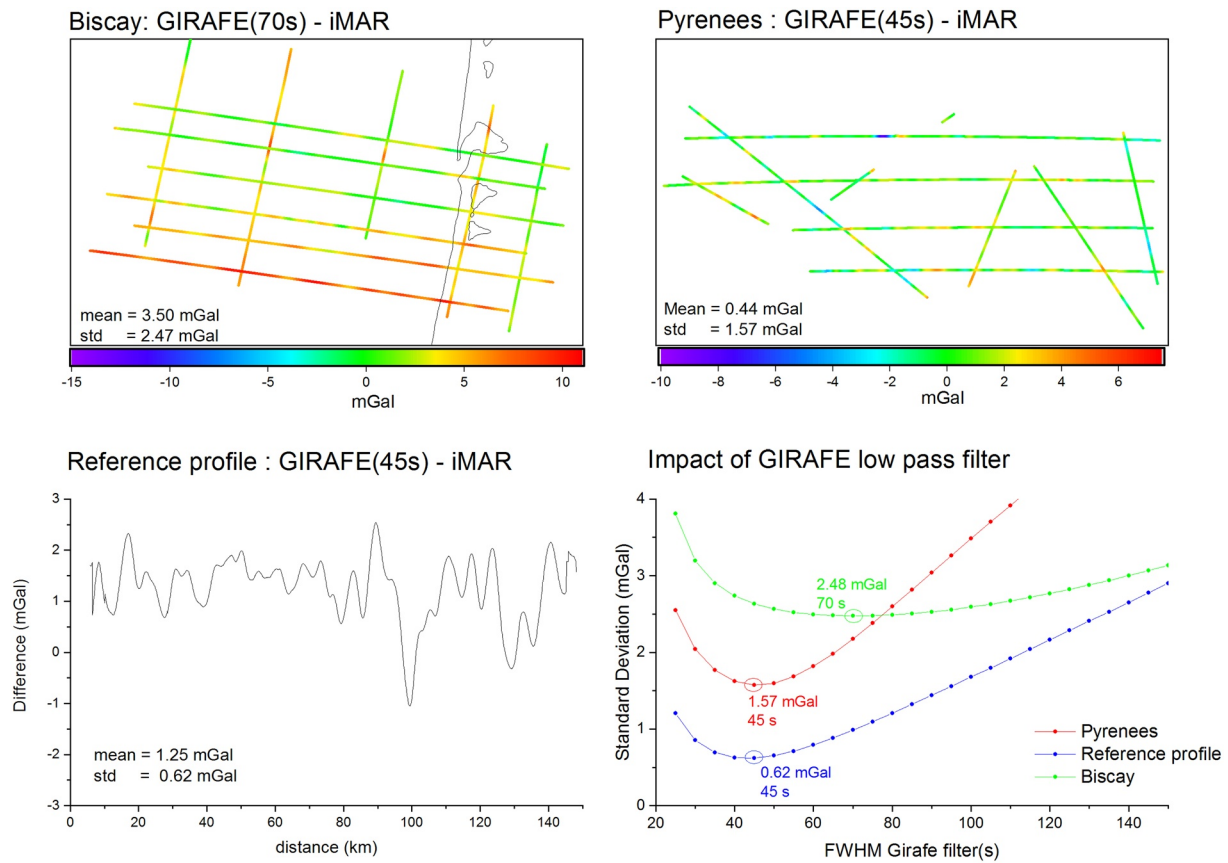


Figure 10. Comparison of gravity disturbance estimated by GIRAFE and iMAR gravimeters. The two upper graphs represent the difference between GIRAFE and iMAR gravity measurements for Bay of Biscay and Pyrenees. The lower-left graph is the difference between the averaged gravity measurements over the reference profile for GIRAFE and iMAR. The lower-right graph shows the standard deviation of the difference between GIRAFE and iMAR measurements versus the filter FWHM pulse response $\Delta\tau$ used for GIRAFE data processing.

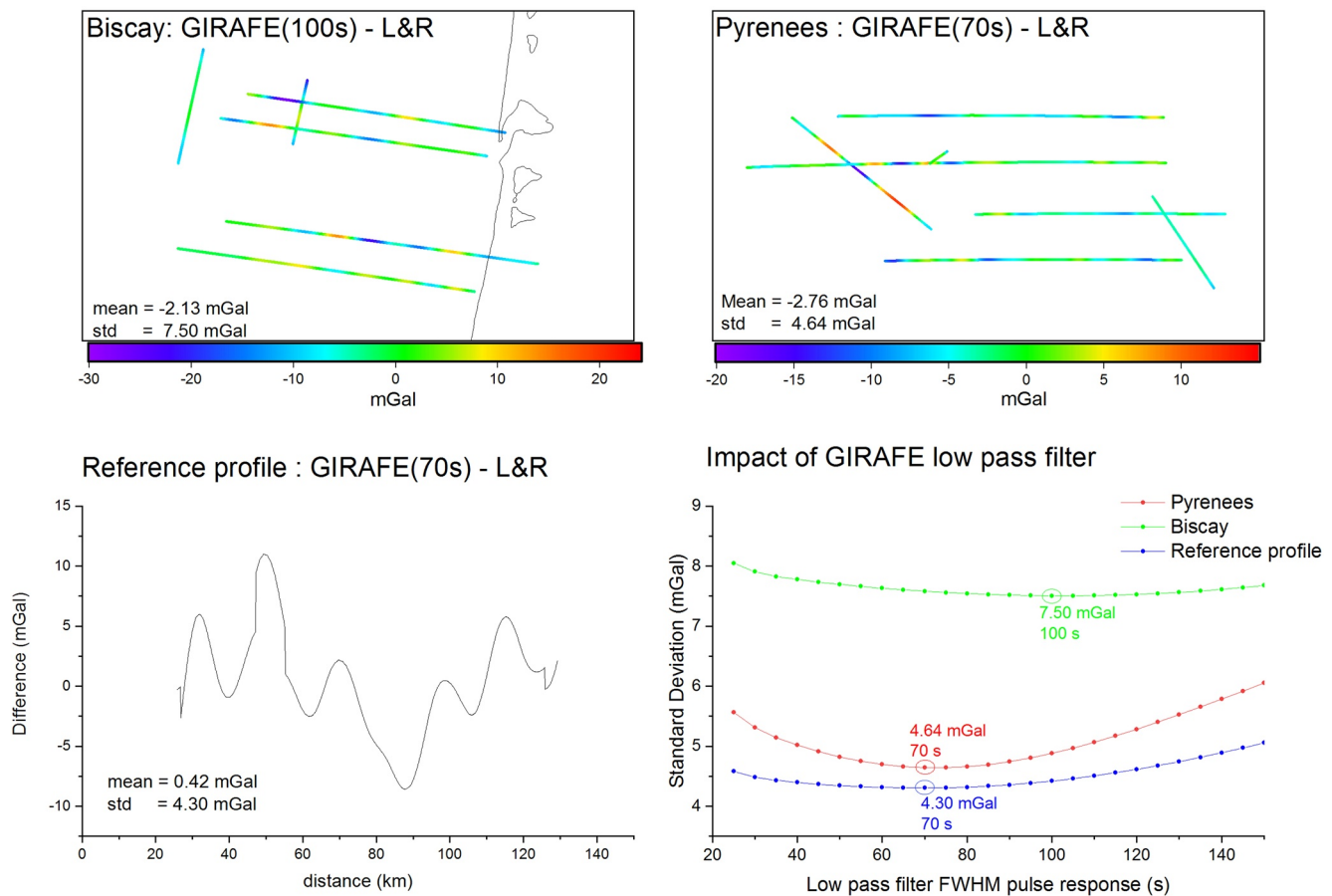


Figure 11. Comparison of gravity disturbance estimated by GIRAFE and L&R gravimeters. The two upper graphs represent the difference between GIRAFE and L&R gravity measurements for Bay of Biscay and Pyrenees. The lower-left graph is the difference between the averaged gravity measurements over the reference profile for GIRAFE and L&R. The lower-right graph shows the standard deviation of the difference between GIRAFE and L&R measurements versus the filter FWHM pulse response $\Delta\tau$ used for GIRAFE data processing.

the averaged profile is equal to the error divided by the square root of the number of pass. For GIRAFE/iMAR comparison, the same values are obtained within 30% validating the estimated error for each gravimeter. For L&R, the comparison of the two approaches was only possible for Pyrenees and reference profile, where it was possible to estimate errors from repeated measurements and lead to less good agreement.

The differences in mean values between the gravity measurements are summarized in Table 4. The difference between iMAR and GIRAFE is in the mGal level for reference profile and Pyrenees (1.25 and 0.44 mGal). However, the difference is larger (3.5 mGal) for Bay of Biscay. The comparison with gravity models (see Section 6.2) suggests that the iMAR estimates are subject to an offset. Concerning L&R gravimeter, the differences are below 1 mGal for the reference profile and between 2 and 6 mGal for Pyrenees and Bay of Biscay.

6. Comparison With Upward-Continued Surface Gravity and Altimetry-Derived Gravity

We use the upward-continued surface gravity as an independent data to validate the airborne gravity measured by the three gravimeters. For this purpose, altimetry-derived gravity data with a spatial resolution of 16 km, shipborne gravity data with a spatial resolution of 1 km and terrestrial gravity data will be used.

Table 4
Standard Deviation and Mean on the Difference Between Gravimeter Measurements (mGal)

		Bay of Biscay	Reference profile	Pyrenees
GIRAFE-iMAR	Std	2.47 (1.87)	0.62 (0.82)	1.57 (1.78)
	Mean	3.50	1.25	0.44
GIRAFE-L&R	Std	7.50	4.30 (2.47)	4.64 (3.80)
	Mean	-2.13	0.42	-2.76
iMAR-L&R	Std	7.72	4.36 (2.47)	5.09 (3.86)
	Mean	-6.30	-0.85	-3.13

Note. The values in parenthesis are the expected standard deviation obtained by summing quadratically each gravimeter error.

6.1. Reference Profile

For the reference profile, the airborne measurements have been compared with Shom marine data acquired in 2018 with the quantum gravimeter GIRAFE, and also with gravity model from satellite altimetry V31 (Sandwell et al., 2014). Marine data and altimetry model have been upward continued to flight altitude using the spectral method of Blakely (1996). In addition, to bring them back to the airborne measurement height reference (WGS84 ellipsoid), the marine data were also corrected to gravity disturbances by the geoid height of the EGM08 model at order 2190 (Pavlis et al., 2012).

The results of the comparison are shown in Figure 12. The airborne gravity disturbance is obtained by averaging over the five passes for iMAR and GIRAFE gravimeters and over two passes for L&R.

Again, the influence of the FWHM pulse response of the filter $\Delta\tau$ used for GIRAFE data processing was studied. For marine data, the standard deviation on the differences is minimum for $\Delta\tau = 40$ s and is equal to 1.05 mGal. For the altimetry model, the standard deviation on the differences is minimum for $\Delta\tau = 55$ s and is equal to 0.95 mGal. The difference of the minimum values could be explained by the higher resolution of the marine gravity data.

GIRAFE and iMAR measurements are in good agreements with gravity models. The differences between GIRAFE have a mean and a standard deviation below or approximately equal to 1 mGal. We notice that the standard deviation between airborne measurements and models (0.9–1 mGal) is bigger than the standard deviation between iMAR and GIRAFE (0.6 mGal). This could be explained by errors on gravity models or common errors on iMAR and GIRAFE measurements, for example, GNSS errors.

For L&R, we obtain a good agreement for the mean value. However, the standard deviation on the difference is bigger (4 mGal) confirming larger measurement errors for L&R compared to iMAR and GIRAFE.

6.2. Bay of Biscay and Pyrenees

The upward continuation estimation of the gravity disturbances at the flight altitude was performed in point-to-point mode with the well-known remove-compute-restore technique. First, the gravity disturbances from the EGM2008 up to degree/order 2190 (Pavlis et al., 2012) were used to remove/restore the long wavelength components in the gravity data. We also used the Residual Terrain Model (RTM) effects (Forsberg, 1984) computed from Digital Terrain Model (DTM) to remove/restore the short wavelengths (beyond degree/order 2190). On the Pyrenees, the 90 m resolution SRTM3arc v4.1 (Farr et al., 2007) was used as the detailed DTM to compute the RTM effects. The 15 in. resolution Digital Bathymetry Model (DBM) SRTM15arc plus (Tozer et al., 2019) was merged with SRTM3arc V4.1 to compute the RTM effects on the Bay of Biscay. Then, the residual gravity disturbances have been upward continued to the flight altitude using the Least-Squares Collocation (LSC) (Forsberg, 1987).

In Figure 13, δg_{res}^{sur} and δg_{res}^{flight} denote surface gravity disturbances (land, marine measurements or altimetry model) and their residual values, respectively. $\delta g_{EGM2008}^{sur}$ and $\delta g_{EGM2008}^{flight}$ are the long-wavelength gravity disturbances at the topographic/sea surface and at the flight altitude, respectively. δg_{RTM}^{sur} and δg_{RTM}^{flight} represent the topographic gravity effects at the topographic/sea surface and at the flight altitude, respectively. Therefore, the long-wavelength components and the topographic gravity are computed at different altitudes in remove and restore procedures. δg_{res}^{UWC} and δg_{res}^{UWC} are upward continued-gravity disturbances and their residual values, respectively. The terrestrial and marine gravity data were provided by the International Gravimetric Bureau (BGI). Fortunately, two study regions have a relatively dense gravity coverage, as shown in Figure 13. The differences between upward continued and the airborne gravity disturbances measured by three gravimeters are shown in Figures 14 and 15.

For the Bay of Biscay, the standard deviation (STD) and the mean value of these differences are clearly smaller for GIRAFE than for iMAR and L&R. We obtained a standard deviation on the differences equal to 2.17 mGal and a mean bias of -2.64 mGal for GIRAFE. A large bias is visible over the sea part relative to the land, which leads the quite bias in the validation result on the Bay of Biscay. To make this clear, we also use the gravity field derived from the latest altimetric satellite model, namely V31, to validate the airborne gravity. Similar to marine gravity, the gravity disturbance derived from V31 model (Sandwell et al., 2014) is also upward continued to the flight altitude. The bias is no longer visible on the marine part, the mean bias being -0.4 mGal on the Bay of Biscay for GIRAFE. The bias is larger for iMAR and L&R (-3.64 and 2.54 mGal, respectively). This confirms once again the advantage of GIRAFE gravimeters over traditional gravimeters.

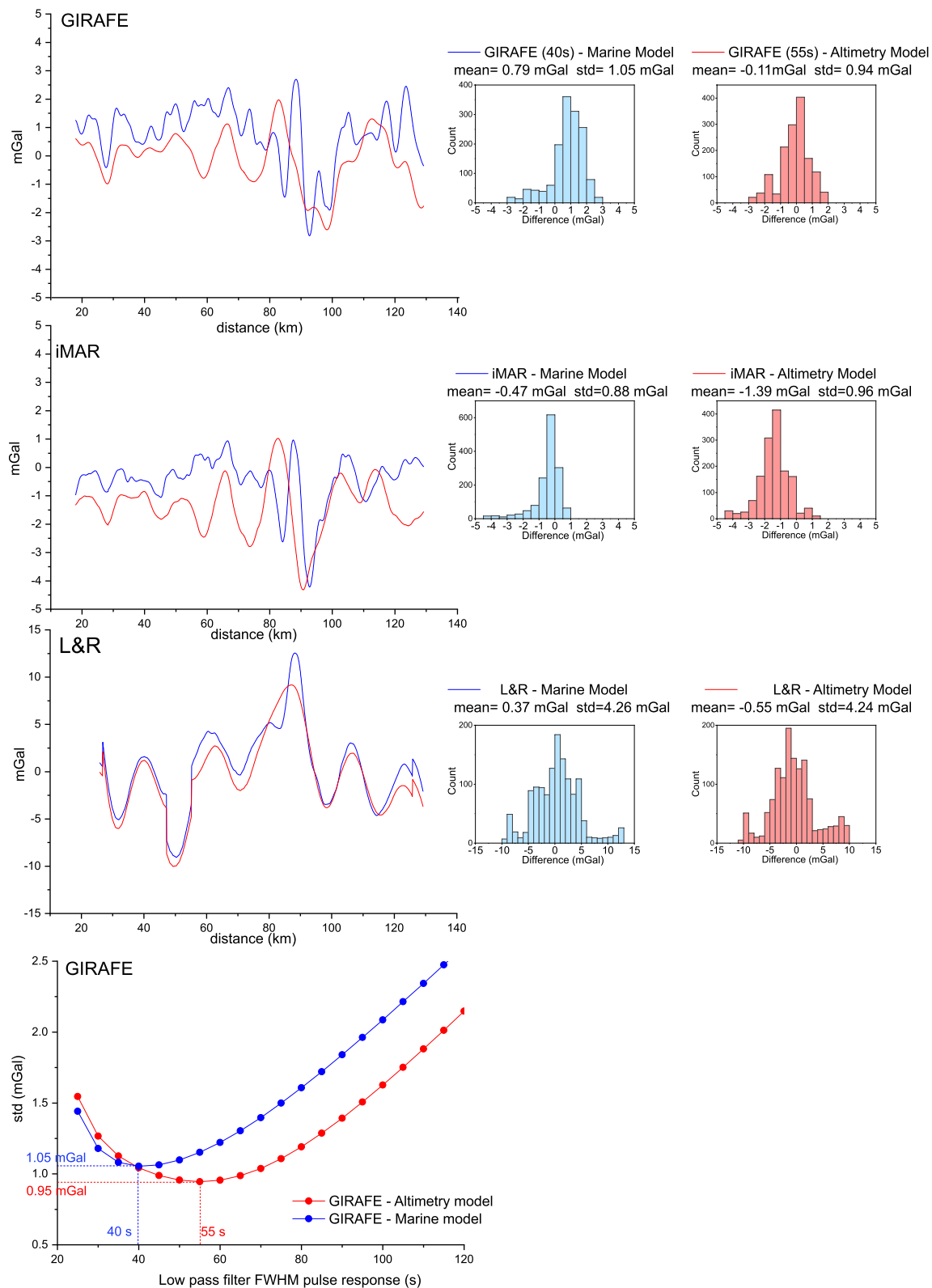


Figure 12. Comparison between airborne measurements and two reference models (marine gravimetry and satellite altimetry). The three upper graphs are the differences between GIRAPE, iMAR, and L&R measurements and the two models. The lowest graph is the standard deviation of the differences between GIRAPE measurements and models versus the FWHM pulse response $\Delta\tau$ of the filter used for GIRAPE data processing.

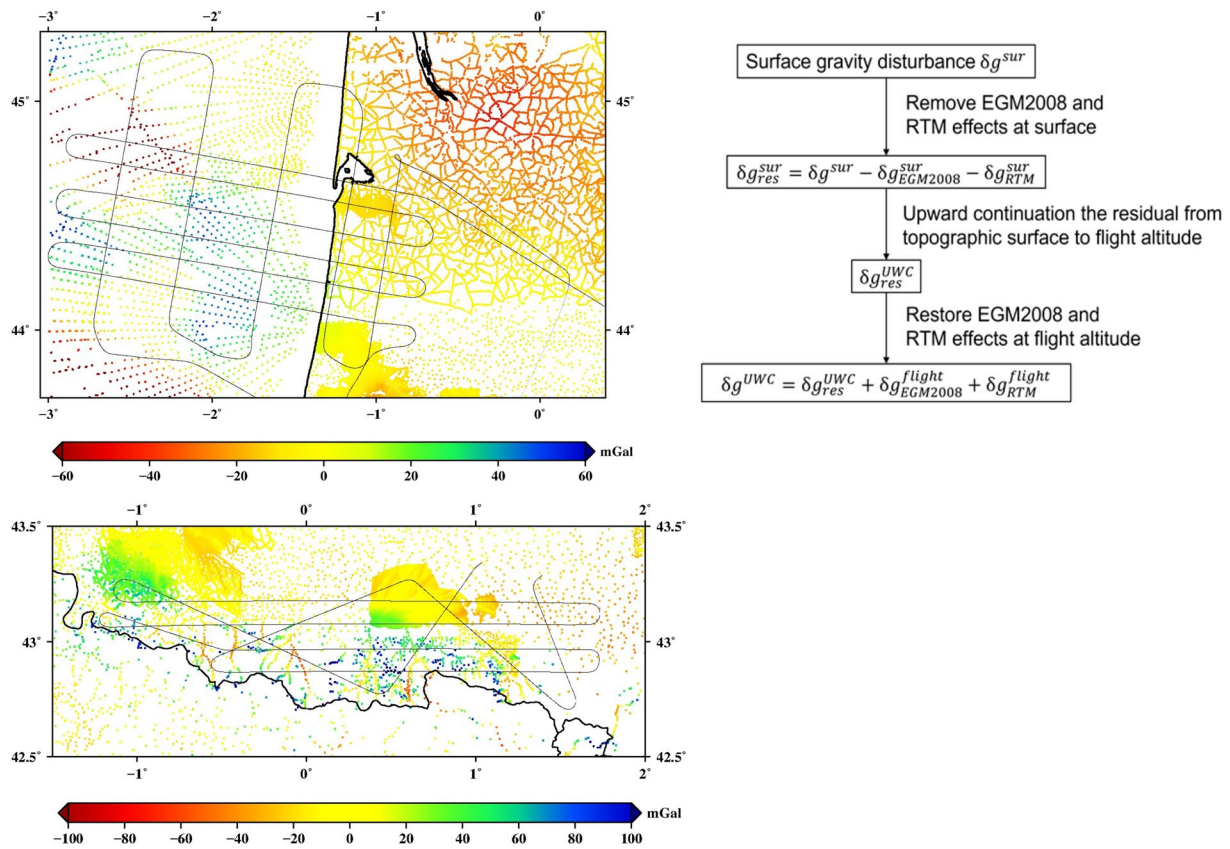


Figure 13. Upper left: Terrestrial and marine gravity data in Bay of Biscay. Lower left: Terrestrial data in Pyrenees. Upper right: Diagram of sequential steps (top to bottom) in the upward continuation of gravity disturbance.

The differences between the upward continued using altimetric gravity and the airborne gravity also reveal that the altimetric gravity is of poor quality in the coastal areas (about 10 km from the coastal line). This explains why the airborne gravimetry is used preferentially to close the gap between gravity data on land and marine altimetric gravity fields. For the Pyrenees, the STD is around 2 mGal for the GIRAFE and iMAR measurements. This indicates that these two measurements are in good agreements with the upward continued-ground gravity disturbances. The L&R measurements have large differences from the upward continued-ground gravity (STD is 5.45 mGal). The smallest mean bias was obtained from GIRAFE (−1.30 mGal); however, this value is quite large. The reason for the large mean bias is in part the reference height inconsistencies, but also inconsistencies in the atmospheric corrections of gravity data, and errors in the upward continuation process. The ground gravity measurements are thus referring to the national height systems, while the airborne gravity is calculated using the height referring to a global height system. Using more than 10,000 GPS/leveling points in France, we have determined that the vertical datum offset of the national height system of France is about 0.87 m (equivalent to 0.3 mGal) with respect to the international (W_0) height system (Sánchez et al., 2016); atmosphere effects are up to 0.8 mGal, and additional errors from linear corrections terms in BGI may also contribute to the bias. It is therefore possible that the GIRAFE bias might be close to zero also over the mountains.

7. Conclusion and Perspectives

In conclusion, we demonstrated absolute airborne gravity measurements with a quantum sensor. From repeated measurements, we estimated measurement errors ranging from 0.6 to 1.3 mGal. Precision measurements have been improved by a factor of 3 compared to the first airborne campaign with the quantum gravimeter. Gravity measurements from two relative gravimeters were acquired simultaneously. The comparison indicated a similar precision between the GIRAFE and iMAR strapdown instruments, whereas the L&R platform system performed poorly in the present flight conditions. We also observed that the long-term stability of GIRAFE gravimeter is

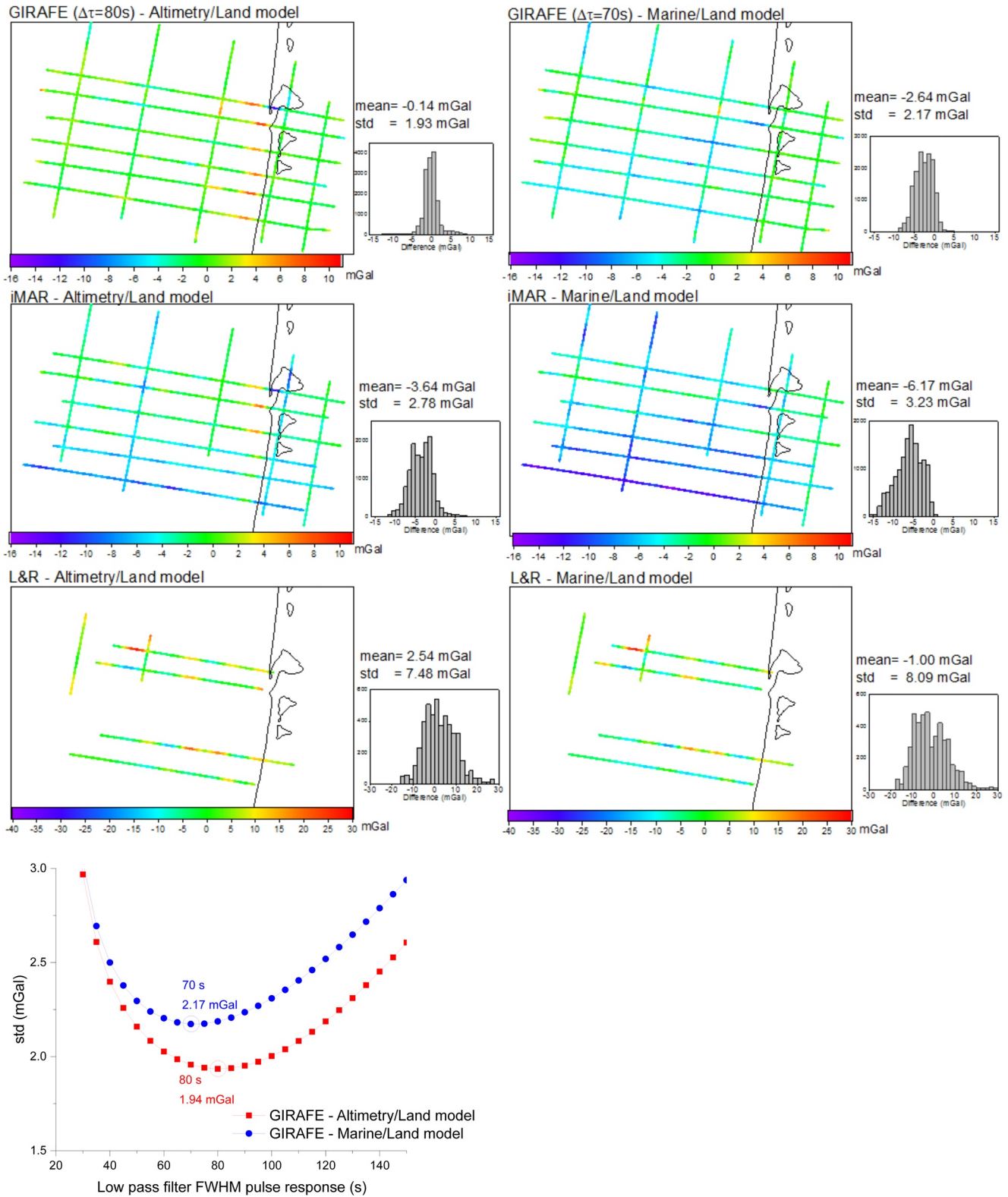


Figure 14. Comparison between gravity disturbance over Bay of Biscay derived from airborne measurements and from gravity models. The six upper graphs represent the difference between airborne measurements (GIRAFE, iMAR, or L&R) and models (Satellite altimetry/Land or Marine/Land). The lowest graph represents the standard deviation of the differences between GIRAFE measurements and models versus the full-width-half-maximum (FWHM) pulse response of the filter $\Delta\tau$ used for GIRAFE data processing.

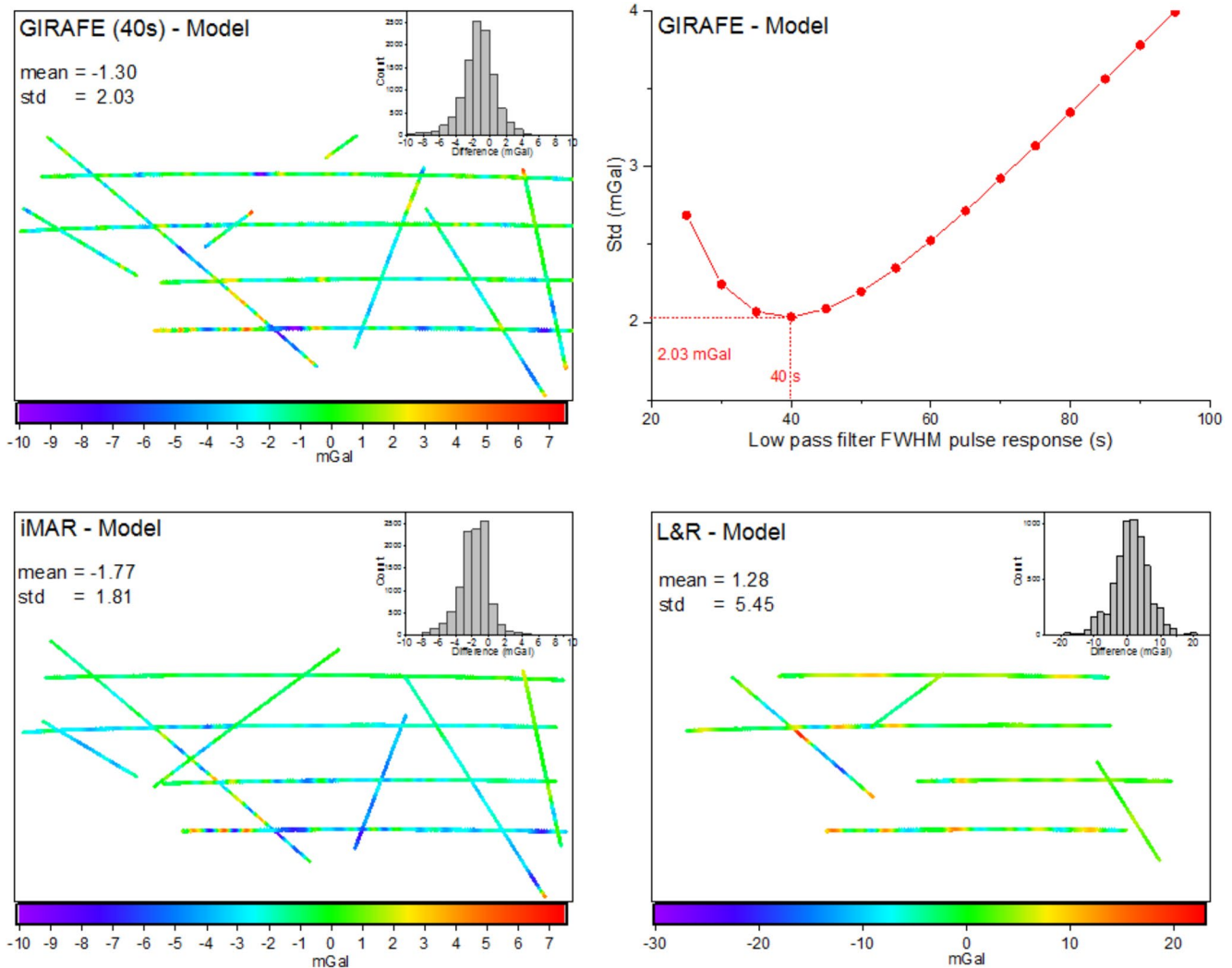


Figure 15. Comparison between gravity disturbances over Pyrenees derived from airborne measurements and from land measurements upward continued. The upper-left graph is the difference between GIRAFE measurements ($\Delta\tau = 40$ s) and the model. The upper-right graph is the standard deviation of the differences between GIRAFE measurements and models versus the full-width-half-maximum (FWHM) pulse response of the filter $\Delta\tau$ used for GIRAFE data processing. The two lower graphs are the difference between iMAR and L&R measurements and the model.

five times better than the iMAR gravimeter. The measurements of the three gravimeters have been compared to gravity models coming from satellite altimetry, marine, and ground measurements. A summary of the comparisons is shown in Figure 16. Good agreements are obtained between GIRAFE, iMAR, and gravity models.

This survey confirms the potential of quantum sensor for airborne gravimetry. Better precision could be achieved in the future with quantum technology. The sensitivity and accuracy of the quantum sensor could still be improved. For example, we could use longer interrogation time, use a more sensitive auxiliary classical accelerometer or use multi-species atom interferometer (Bonnin et al., 2018). On the other hand, data processing has also to be improved. For example, a Kalman filter approach could be used to process quantum gravity measurements. Moreover, GNSS precision is expected to be improved in the future with the increasing of available constellations. With these improvements, we could hope to reach the precision to access to time-variable gravity signals with application in earthquake, volcano, glacier, or groundwater changes.

The second point of improvement is the miniaturization of the sensors in order to have access to smaller carriers like drones. This could be achieved by miniaturizing the control cabinet and by designing, as for the iMAR gravimeter, a strapdown gravimeter that does not need gyrostabilized platform. This could be possible by gyrostabilizing the mirror retroreflecting the laser during the atom interrogation time (Lan et al., 2012). Three axes

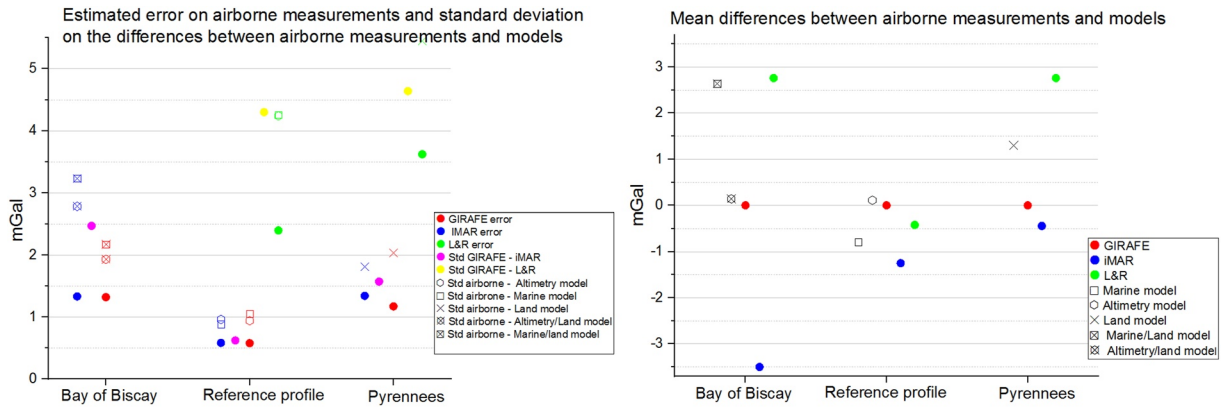


Figure 16. Summary of the intercomparison between GIRAFE, iMAR, and L&R airborne gravity measurements and gravity models. Left: Estimated error on airborne measurements and standard deviation on the differences between airborne measurements and models. Right: Mean differences between airborne measurements and models. The reference value is GIRAFE measurements.

accelerometers combining one vertical and two horizontal atom accelerometers (Bernard et al., 2022; Perrin et al., 2019) could be also of interest for strapdown gravimetry. This configuration could be also very promising for vectorial gravimetry where the horizontal components of the gravity field are also estimated.

Appendix A: Data Processing and Gravity Estimation

A1. Kinematic Acceleration and Eötvös Effect

Both classical and quantum gravimeters measure specific force, f , which is a combination of gravity acceleration, kinematic acceleration, and coupling to Earth rotation (Eötvös effect). This may be expressed as

$$f = g + \ddot{h} - a_{\text{Eöt}}, \quad (\text{A1})$$

where g is the gravity acceleration (g is positive when downward), \ddot{h} is the time second derivative of h the ellipsoidal height (h is positive when upward) and represents the vertical kinematic acceleration of the aircraft. The centrifugal component due to Earth's rotation has been absorbed by the gravity term, g . The Eötvös term $a_{\text{Eöt}}$ can be expressed as (Heiskanen & Moritz, 1967):

$$a_{\text{Eöt}} = 2 \omega_E \cos \varphi v_E + \left[\frac{v_E^2}{N(\varphi) + h} + \frac{v_N^2}{M(\varphi) + h} \right], \quad (\text{A2})$$

with

$\omega_E = 7.292115 \cdot 10^{-5} \text{ s}^{-1}$:	Earth's rotation rate (inertial frame)
φ	:	Geodetic latitude
v_E	:	East velocity
v_N	:	North velocity
h	:	Ellipsoidal height
$M(\varphi) = \frac{a^2 \cdot b^2}{(a^2 \cos(\varphi)^2 + b^2 \sin(\varphi)^2)^{3/2}}$:	Earth's radius of curvature in the (north-south) meridian
$N(\varphi) = \frac{a^2}{(a^2 \cos(\varphi)^2 + b^2 \sin(\varphi)^2)^{1/2}}$:	Earth's radius of curvature in the prime vertical
$a = 6378137.0 \text{ m}$:	Earth's equatorial radius (WGS84)
$b = 6356752.3 \text{ m}$:	Earth's polar radius (WGS84)

The Eötvös effect represents two additional fictitious forces that arise during horizontal (north/east) motion on the surface of the Earth. The first term is the Coriolis force which can be interpreted as an apparent increase or decrease in Earth's centrifugal force due to east/west motion. The other term is known as the transport-rate effect, which arises due to the change in orientation of the vertical direction (along the ellipsoidal normal) as one moves across the Earth.

A2. GNSS Data Processing

The GNSS observations were sampled at 1 Hz and processed using the Waypoint commercial software suite from Hexagon/NovAtel along with precise ephemerides from the Center for Orbit Determination in Europe. The software utilizes a Kalman filter to derive position estimates using a Precise Point Positioning approach. These estimates can be translated from the GNSS antenna to the position of any other instrument on board the aircraft if the lever arm (instrument-antenna separation) is known. Assuming that the lever arm, \mathbf{l}^b , is specified along the front, right and down directions of the aircraft (body frame) and is positive in the direction from the instrument to the GNSS antenna, the position can be translated using the aircraft attitude as

$$\mathbf{p}_{\text{sensor}} = \mathbf{p}_{\text{GNSS}} - \mathbf{T} \mathbf{C}_b^n \mathbf{l}^b, \quad (\text{A3})$$

where $\mathbf{p} = [\varphi, \lambda, h]$ denotes the position in geodetic coordinates, \mathbf{C}_b^n is the body-to-navigation-frame transformation matrix and \mathbf{T} is the Cartesian-to-curvilinear transformation matrix as

$$\mathbf{C}_b^n = \begin{bmatrix} \cos \beta \cos \gamma & -\cos \alpha \sin \gamma & \sin \alpha \sin \gamma \\ \cos \beta \sin \gamma & \cos \alpha \cos \gamma & -\sin \alpha \cos \gamma \\ -\sin \beta & \sin \alpha \cos \beta & \cos \alpha \cos \beta \end{bmatrix} \quad (\text{A4})$$

where α , β , and γ denote the bank, elevation, and heading angle, respectively, and

$$\mathbf{T} = \begin{bmatrix} \frac{1}{M(\varphi)+h} & 0 & 0 \\ 0 & \frac{1}{(N(\varphi)+h)\cos \varphi} & 0 \\ 0 & 0 & 1 \end{bmatrix}. \quad (\text{A5})$$

The kinematic and Eötvös accelerations in Equation A1 are derived from these translated GNSS position estimates using a central finite difference estimator.

A3. Gravity Disturbance Calculation

The gravity disturbance is obtained by subtracting the GRS80 normal gravity model taking into account height and latitude effects (Torge & Müller, 2012):

$$g_0 = \frac{a \cdot g_E \cdot \cos(\varphi)^2 + b \cdot g_P \cdot \sin(\varphi)^2}{\sqrt{a^2 \cdot \cos(\varphi)^2 + b^2 \cdot \sin(\varphi)^2}} \cdot (1 + \Gamma_1 \cdot h + \Gamma_2 \cdot h^2)$$

with:

$$\begin{aligned}
 g_E &= 9.78032677 \text{ m s}^{-2} \text{ (GRS80)} \\
 g_P &= 9.83218637 \text{ m s}^{-2} \text{ (GRS80)} \\
 \Gamma_1 &= -\frac{2}{a} \left(1 + f + \frac{a^2 \cdot b \cdot \omega_E^2}{GM} - 2 \cdot f \cdot \sin(\varphi)^2 \right) \\
 \Gamma_2 &= \frac{3}{a^2} \\
 f &= \frac{a - b}{a} \\
 GM &= 3.986005 \cdot 10^{14} \text{ m}^3 \text{ s}^{-3} \text{ (GRS80)} \\
 a &= 6378137.0 \text{ m : Earth's equatorial radius (GRS80)} \\
 b &= 6356752.3 \text{ m : Earth's polar radius (GRS80)}
 \end{aligned} \tag{A6}$$

This computes the ellipsoidal gravity in the GRS80 system.

A4. GIRAFE Quantum Gravimeter

The data processing and gravity estimation from the quantum gravimeter measurements and GNSS data are similar to the one used for our last airborne campaign (Bidel et al., 2020). The main difference comes from the low pass filter, where a Gaussian filter is used instead of a Bessel fourth-order filter. We also here do not correct alignment error of the platform. Indeed, during this campaign, the estimated error alignment of the platform is small (≤ 1.5 mrad) and the correction is not pertinent.

The Gaussian low pass filter used for the data processing is implemented in the Fourier domain. The FFT of the data is multiplied by the Gaussian function:

$$h(\omega) = \exp\left(-\frac{\omega^2 \sigma_t^2}{2}\right) \tag{A7}$$

To minimize border effects, the input signal of the filter is extended from both sides with the symmetrical signal. In the time domain, this is equivalent to convolute the data by a Gaussian function equal to

$$h(t) = \frac{1}{\sqrt{2\pi}\sigma_t} \exp\left(-\frac{t^2}{2\sigma_t^2}\right) \tag{A8}$$

$h(t)$ represents the response of the filter to a Dirac function. The filter is characterized by the full-width-half-maximum (FWHM) of this function which is equal to $\Delta\tau = \sqrt{8 \ln(2)}\sigma_t$. For a plane of velocity v , this gives a spatial resolution equal to $\Delta x = v \Delta\tau$.

The GNSS data and gravimeter data are first filtered by a $\Delta t = 7$ s low pass Gaussian filter. Then, the gravimeter data at 10 Hz are linearly interpolated on the time vector of GNSS data at 1 Hz. Before interpolation, the precise delay between GNSS and gravimeter data is adjusted to obtain the best correlation between acceleration measured from the gravimeter and acceleration derived from GNSS data. The delay is adjusted with a precision of 10 ms and is found to be constant for each flight. Then we select measurements acquired during plane straight trajectory that is, with a yaw rotation rate below 0.2 mrad/s. The measurements during change of direction do not allow precise gravity measurements and could perturb by border effect the gravity measurements in straight line. The gravimeter measurements are corrected for kinematic and Eötvös acceleration. Finally, a Gaussian low pass filter is applied with an FWHM pulse response ranging from 25 to 200 s.

A5. The L&R Platform Gravimeter

The L&R sensor is mounted on a two-axis damped platform that keeps the sensitive axis of the gravimeter approximately aligned with the direction of the gravity vector, that is, the plumb line. To derive gravity estimates, the specific force observations, f , are corrected for kinematic and Eötvös accelerations according to Equations A1 and A2. To transition from relative to absolute gravity estimates, a base reading, g_{base} , performed before the flight is subtracted from the observations and an external tie value, g_{tie} , is added to the observations as

$$g = f - \ddot{h} + a_{E\ddot{o}t} + \delta g_{\text{tilt}} + (g_{\text{tie}} - g_{\text{base}}). \quad (\text{A9})$$

To correct for any sensor misalignment, a tilt correction, δg_{tilt} , is introduced. A pair of accelerometers mounted on top of the sensor casing along the long-axis and cross-axis of motion are exploited to estimate the tilt angle of the sensor. Assuming that the long-axis accelerometer is tilted by an angle, ϕ_{long} , the observed accelerations will represent a component of gravity, g , and a component of kinematic acceleration, q_{long} , projected onto the sensitive axis as

$$f_{\text{long}} = g \sin \phi_{\text{long}} + q_{\text{long}} \cos \phi_{\text{long}} \approx g \phi_{\text{long}} + q_{\text{long}}, \quad (\text{A10})$$

where small angle approximations are introduced. The kinematic acceleration, q_{long} , is derived from GNSS position estimates, projected onto the direction of travel and corrected for a horizontal Eötvös effect. An estimate of the long-axis tilt angle is therefore

$$\phi_{\text{long}} \approx \frac{f_{\text{long}} - q_{\text{long}}}{g_0}, \quad (\text{A11})$$

where the standard value of gravity, $g_0 = 9.80665 \text{ m/s}^2$, is used. Similar arguments hold for the cross-axis direction. From the estimated tilt angles, a tilt correction is formed as (Olesen, 2003, eq. 2.11):

$$\delta g_{\text{tilt}} = (1 - \cos \phi_{\text{long}} \cos \phi_{\text{cross}}) f + \sin \phi_{\text{long}} f_{\text{long}} + \sin \phi_{\text{cross}} f_{\text{cross}}, \quad (\text{A12})$$

which is derived under the assumption of small tilt angles. Following these corrections, the gravity estimates are filtered using a threefold forward/backward zero-phase Butterworth filter with a (full-width) half power point of 134 s in the temporal domain. At an along-track velocity of 100 m/s, this corresponds to an FWHM spatial resolution of approximately 13.4 km. The relatively heavy filtering of the gravimeter observations was necessitated by the relatively turbulent flights, compared to earlier campaigns (Forsberg & Olesen, 2010).

A6. The iMAR Strapdown Gravimeter

The temperature stabilized IMU from iMAR Navigation was mounted in a strapdown configuration, meaning that the sensor casing is rigidly mounted to the chassis of the aircraft. The observations of the internal accelerometers and gyroscopes are sequentially integrated in a dead reckoning methodology to form independent estimates of attitude, velocity, and heading. Because errors are integrated and will continue to increase using this approach, the navigation estimates are continuously corrected and the sensor biases are calibrated in a Kalman filter framework by introducing GNSS position estimates. The state vector used in the Kalman filter is

$$\delta \mathbf{x} = [\delta \boldsymbol{\psi}, \delta \mathbf{v}, \delta \mathbf{p}, \delta \mathbf{b}_g, \delta \mathbf{b}_a, \delta \Delta \mathbf{g}, \delta \Delta \dot{\mathbf{g}}, \delta \Delta \ddot{\mathbf{g}}]^\top, \quad (\text{A13})$$

where $\boldsymbol{\psi}$, \mathbf{v} , and \mathbf{p} denote the attitude, velocity, and position, respectively, \mathbf{b}_g and \mathbf{b}_a denote the gyroscope and accelerometer biases, respectively, and $\Delta \mathbf{g}$ denotes the anomalous/disturbing gravity vector, with respect to the gravity model used to correct specific force observations during processing. In the above, dots denote derivative with respect to time and δ indicates an error-state implementation, meaning that the Kalman filter estimates errors on the inertial navigation solution, rather than full quantities.

The temporal evolution of the error-state vector, $\delta \mathbf{x}$, is described by a linear dynamic system model

$$\delta \dot{\mathbf{x}}(t) = \mathbf{F}(t) \delta \mathbf{x}(t) + \mathbf{G}(t) \mathbf{w}_s(t), \quad (\text{A14})$$

containing a white noise vector, \mathbf{w}_s , and system noise distribution matrix, \mathbf{G} , allowing the user to model sensor errors and their distribution onto the state variables. Additionally, the (re-)distribution of errors is determined by the motion-dependent system matrix

$$\mathbf{F} = \begin{bmatrix} \mathbf{F}_{11}^n & \mathbf{F}_{12}^n & \mathbf{F}_{13}^n & \mathbf{0}_3 & \mathbf{C}_b^n & \mathbf{0}_3 & \mathbf{0}_3 & \mathbf{0}_3 & \mathbf{0}_3 \\ \mathbf{F}_{21}^n & \mathbf{F}_{22}^n & \mathbf{F}_{23}^n & \mathbf{C}_b^n & \mathbf{0}_3 & \mathbf{I}_3 & \mathbf{0}_3 & \mathbf{0}_3 & \mathbf{0}_3 \\ \mathbf{0}_3 & \mathbf{F}_{32}^n & \mathbf{F}_{33}^n & \mathbf{0}_3 & \mathbf{0}_3 & \mathbf{0}_3 & \mathbf{0}_3 & \mathbf{0}_3 & \mathbf{0}_3 \\ \hline \mathbf{0}_3 & \mathbf{0}_3 \\ \mathbf{0}_3 & \mathbf{0}_3 \\ \hline \mathbf{0}_3 & \mathbf{0}_3 & \mathbf{0}_3 & \mathbf{0}_3 & \mathbf{0}_3 & \mathbf{0}_3 & \mathbf{I}_3 & \mathbf{0}_3 & \mathbf{0}_3 \\ \mathbf{0}_3 & \mathbf{I}_3 & \mathbf{0}_3 \\ \mathbf{0}_3 & \mathbf{0}_3 & \mathbf{0}_3 & \mathbf{0}_3 & \mathbf{0}_3 & -\beta^3 & -3\beta^2 & -3\beta & \mathbf{0}_3 \end{bmatrix}, \quad (\text{A15})$$

with the elements of the upper left corner listed in Groves (2013, eqs. 14.64–14.71), \mathbf{C}_b^n is the transformation matrix from the body-frame to navigation-frame and β is a 3×3 diagonal matrix containing temporal correlation parameters of the gravity anomaly vector.

The differential Equation A14 is essentially solved for in each propagation interval between subsequent GNSS position estimates. This allows for the forward propagation of an error covariance matrix, \mathbf{P} , which is associated with the inertial navigation estimates. Since both the inertial and GNSS navigation estimates now have an associated error covariance matrix, these can be combined in a statistically optimal fashion by forming the Kalman filter gain

$$\mathbf{K} = \frac{\mathbf{P}\mathbf{H}^T}{\mathbf{H}\mathbf{P}\mathbf{H}^T + \mathbf{R}}, \quad (\text{A16})$$

where \mathbf{R} is the error covariance of the GNSS position estimates and \mathbf{H} is a measurement matrix, relating the state variables to the observations (position estimates). The error state vector, $\delta\mathbf{x}$, and error covariance matrix, \mathbf{P} , is then updated by forming the measurement innovation, $\delta\mathbf{z}$, as the difference between inertial and GNSS navigation estimates:

$$\delta\mathbf{x} = \mathbf{K} \delta\mathbf{z} = \mathbf{K} \left(\mathbf{p}_{\text{GNSS}} - \mathbf{H} \begin{bmatrix} \boldsymbol{\psi}_{\text{IMU}} \\ \mathbf{v}_{\text{IMU}} \\ \mathbf{p}_{\text{IMU}} \\ \mathbf{0}_{15 \times 3} \end{bmatrix} \right) \quad (\text{A17})$$

$$\mathbf{P}^{\text{updated}} = \mathbf{P} - \mathbf{K}(\mathbf{H}\mathbf{P}).$$

Once the errors on the state variables, $\delta\mathbf{x}$, are estimated, these are used to correct the inertial navigation estimates before continuing the dead reckoning navigation approach and to correct any sensor output for systematic errors, that is, sensor bias. This is denoted as a closed-loop implementation of the Kalman filter and results in combined IMU/GNSS estimates of attitude, velocity, position, and sensor biases. The attitude estimates are used in the computation of any Eötvös and tilt effects, but the combined IMU/GNSS navigation solution should not be used to derive kinematic accelerations.

Since the error on the gravitational model used in processing is estimated in the Kalman filter, these error estimates can be added back to the model to arrive at gravity estimates. In this case, the temporal along-track evolution of the gravity disturbance is modeled as a third-order Gauss-Markov process, with a standard deviation, σ_{GM3} , and correlation parameter, β_{GM3} , which essentially controls the degree of smoothing the gravity estimates. These parameters are part of the system noise vector, \mathbf{w}_s , and system matrix, $\mathbf{F}(t)$, where the correlation matrix is formed as

$$\boldsymbol{\beta} = \begin{bmatrix} \beta_N & 0 & 0 \\ 0 & \beta_E & 0 \\ 0 & 0 & \beta_D \end{bmatrix} = |v_{\text{hor}}| \begin{bmatrix} \beta_{N,\text{GM3}} & 0 & 0 \\ 0 & \beta_{E,\text{GM3}} & 0 \\ 0 & 0 & \beta_{D,\text{GM3}} \end{bmatrix}, \quad (\text{A18})$$

using the along-track velocity, $|v_{\text{hor}}|^2 = v_N^2 + v_E^2$, to convert from spatial to temporal domains. The final estimates are derived by running the Kalman filter both forward and backward in time and combining these using a Rauch-Tung-Striebel smoother (Gelb, 1974, chapter 5). In this approach, no further smoothing of the gravity estimates is needed.

Appendix B: Quantitative Comparison of GIRAFE, iMAR, and L&R Precisions

In this appendix, we calculate and analyze the statistics of repeated gravity measurements performed at the same location to compare the precision of GIRAFE, iMAR, and L&R gravimeters. For Pyrenees and Bay of Biscay surveys, the data sets are:

$$\delta g_1^k(r_n) - \delta g_2^k(r_n) \quad (\text{B1})$$

with r_n are the locations of the crossing points and $\delta g_{1(2)}^k$ is the gravity disturbance measured at the first (second) pass by the gravimeter $k = \text{GIRAFE, iMAR, or L\&R}$. For the reference profile survey, the data sets are:

$$\delta g_i^k(r_0 + n\Delta r) - \delta g_j^k(r_0 + n\Delta r) \text{ with } i, j = 1, 2, 3, 4 \text{ or } 5 \text{ and } i > j \quad (\text{B2})$$

where δg_i^k is the gravity disturbance measured at the i th pass by the gravimeter $k = \text{GIRAFE, iMAR, or L\&R}$ at location $r_0 + n\Delta r$ along the profile. r_0 is the location of the beginning of the profile and Δr is the distance step along the profile. This distance has been chosen equal to 4.5 km, which corresponds to the FWHM spatial resolution of the filter used in GIRAFE data processing.

First, we test the statistical independence of data samples by calculating the Pearson correlation coefficients which measure linear correlations (see Table B1). We obtain between GIRAFE and iMAR data sets a significant correlation for the reference profile and Pyrenees and no significant correlation for Bay of Biscay. We do not obtain significant correlations between L&R and GIRAFE or iMAR. These observed correlations may come from GNSS errors which act on the gravity estimations of all three gravimeters. These correlations show up only for the data that have the smallest measurement errors and therefore in which the relative contribution of GNSS errors should be more important. This correlation analysis may suggest that GNSS errors are not negligible for iMAR and GIRAFE gravity measurements.

Second, we test the normality of the data samples using the Shapiro-Wilk method. The results given in Table B2 show that GIRAFE and iMAR data sets for reference profile clearly deviate from a normal distribution. In the other cases, data sets do not deviate significantly from a normal distribution.

Third, we test for the homogeneity of variances so as to estimate if the variances of each data sample are significantly different. We use an F -test of equality of variances which assumes normal distribution. The results for iMAR and GIRAFE reference profile in which data sets do not follow a normal distribution should thus be taken with caution. The results of the test reported in Table B3 show that the variance of iMAR and GIRAFE data sets are not significantly different. We observe, however, a significantly higher variance for L&R data sets.

Finally, we test the homogeneity of the expected values for iMAR and GIRAFE data sets which have no significantly different variances. We use for that a one-sample t -test for each gravimeter data set and a two-sample t -test. The results given in Table B4 show that for the reference profile the mean of iMAR data set is significantly different from 0, while the mean of GIRAFE data set is no significantly different from 0. For Pyrenees and Bay of Biscay, we do not observe significantly of a mean different from zero for iMAR and GIRAFE. A nonzero value of the mean can be interpreted as a drift of the gravity measurements. Indeed, we always calculate the difference in the same way (early measurement – later measurement). The mean value significantly different from 0 obtained on the reference profile underlines the drift of iMAR measurements.

Table B1
Linear Correlation Coefficients Between Repeated Measurements Differences From Different Gravimeters

	Bay of Biscay			Reference profile			Pyrenees		
	corr.	p Value	N	corr.	p Value	N	corr.	p Value	N
GIRAFE-iMAR	0.071	0.73	26	0.252	$2 \cdot 10^{-5}$	277	0.482	0.059	16
GIRAFE-L&R	–	–	2	0.097	0.68	20	–	–	3
L&R-iMAR	–	–	2	–0.048	0.84	20	–	–	4

Note. corr. is the Pearson correlation coefficient. P value is the probability of obtaining correlation coefficients at least as extreme as the correlation coefficient actually observed, under the assumption of no correlation. N is the number of sample in the data set.

Table B2
Shapiro-Wilk Test of Normality

	Bay of Biscay		Reference profile		Pyrenees	
	<i>p</i> Value	<i>N</i>	<i>p</i> Value	<i>N</i>	<i>p</i> Value	<i>N</i>
GIRAFE	0.12	30	0.0056	340	0.36	17
iMAR	0.48	26	$7.6 \cdot 10^{-5}$	277	0.78	18
L&R	–	2	0.10	20	–	4

Note. *p* value is the probability of obtaining data sets at least as extreme as the data sets actually observed, under the assumption of a normal distribution. *N* is the number of sample in the data set.

Table B3
Homogeneity of Variance Test

	Bay of Biscay			Reference profile			Pyrenees		
	Ratio	<i>p</i> value	<i>N</i>	Ratio	<i>p</i> value	<i>N</i>	Ratio	<i>p</i> value	<i>N</i>
GIRAFE-iMAR	1.053	0.89	26	1.078	0.53	277	0.561	0.27	16
GIRAFE-L&R	–	–	2	0.133	$5 \cdot 10^{-5}$	20	–	–	3
iMAR/L&R	–	–	2	0.096	$4 \cdot 10^{-6}$	20	–	–	4

Note. Ratio is the ratio of variance between the two gravimeters data sets. *p* Value is the probability of obtaining a ratio of variance at least as extreme as the ratio actually observed, under the assumption of equal variance. *N* is the number of sample in the data set.

Table B4
Homogeneity of Expected Values

	Bay of Biscay			Reference profile			Pyrenees		
	Mean	<i>p</i> Value	<i>N</i>	Mean	<i>p</i> Value	<i>N</i>	Mean	<i>p</i> value	<i>N</i>
GIRAFE	–0.37	0.29	30	0.16	0.10	340	0.97	0.011	17
iMAR	0.14	0.72	26	–0.96	$4 \cdot 10^{-18}$	277	0.79	0.08	18
GIRAFE-iMAR	–0.52	0.35	26	1.11	$3 \cdot 10^{-13}$	277	–0.16	0.77	16

Note. Mean is the mean value given in mGal. *p* Value is the probability of obtaining a mean at least as extreme as the mean actually observed, under the assumption of a mean value equal to 0. *N* is the number of sample in the data set.

Data Availability Statement

The data supporting the reported research are available from the Zenodo repository (<https://doi.org/10.5281/zenodo.7245500>).

References

- Berman, P. R. (1997). *Atom interferometry*. Academic Press.
- Bernard, J., Bidet, Y., Cadoret, M., Salducci, C., Zahzam, N., Schwartz, S., et al. (2022). Atom interferometry using σ^+ - σ -Raman transitions between $f=1, m_f = \pm 1$ and $f=2, m_f = \mp 1$. *Physical Review A*, *105*(3), 033318.
- Bidet, Y., Zahzam, N., Blanchard, C., Bonnin, A., Cadoret, M., Bresson, A., et al. (2018). Absolute marine gravimetry with matter-wave interferometry. *Nature Communications*, *9*(1), 627. <https://doi.org/10.1038/s41467-018-03040-2>
- Bidet, Y., Zahzam, N., Bresson, A., Blanchard, C., Cadoret, M., Olesen, A. V., & Forsberg, R. (2020). Absolute airborne gravimetry with a cold atom sensor. *Journal of Geodesy*, *94*(2), 20. <https://doi.org/10.1007/s00190-020-01350-2>
- Blakely, R. J. (1996). *Potential theory in gravity and magnetic applications*. Cambridge University Press.
- Bonnin, A., Diboune, C., Zahzam, N., Bidet, Y., Cadoret, M., & Bresson, A. (2018). New concepts of inertial measurements with multi-species atom interferometry. *Applied Physics B*, *124*(9), 181. <https://doi.org/10.1007/s00340-018-7051-5>

Acknowledgments

The development of the ONERA quantum gravimeter GIRAFE was funded by ONERA, the French Defense Agency (DGA), and Shom. The airborne campaign was carried out with support from CNES (Project no. 3673; Bonvalot et al., 2018) and ESA. The authors thank SAFIRE for their excellent support for the flights and the installation of the complex system in the ATR-42.

- Bonvalot, S., Lalancette Lequentrec, M.-F., Bresson, A., Bidel, Y., Zahzam, N., & Bruinsma, S. (2018). *Girafe-airgravi: Potentiel d'un gravimètre interférométrique embarqué pour la géodésie, la géophysique et l'océanographie*. cnes toasca project n° 3673. CNES Paris.
- Carraz, O., Lienhart, F., Charrière, R., Cadoret, M., Zahzam, N., Bidel, Y., & Bresson, A. (2009). Compact and robust laser system for onboard atom interferometry. *Applied Physics B*, 97(2), 405–411. <https://doi.org/10.1007/s00340-009-3675-9>
- Farr, T. G., Rosen, P. A., Caro, E., Crippen, R., Duren, R., Hensley, S., et al. (2007). The shuttle radar topography mission. *Reviews of Geophysics*, 45(2), RG2004. <https://doi.org/10.1029/2005rg000183>
- Forsberg, R. (1984). *A study of terrain reductions, density anomalies and geophysical inversion methods in gravity field modelling*. (Tech. Rep. No. 355). Ohio State University Columbus Department of Geodetic Science and Surveying.
- Forsberg, R. (1987). A new covariance model for inertial gravimetry and gradiometry. *Journal of Geophysical Research*, 92(B2), 1305–1310. <https://doi.org/10.1029/jb092ib02p01305>
- Forsberg, R., & Olesen, A. V. (2010). Airborne gravity field determination. In *Sciences of geodesy-I* (pp. 83–104). Springer.
- Freier, C., Hauth, M., Schkolnik, V., Leykauf, B., Schilling, M., Wziontek, H., et al. (2016). Mobile quantum gravity sensor with unprecedented stability. *Journal of Physics: Conference Series*, 723, 012050. <https://doi.org/10.1088/1742-6596/723/1/012050>
- Gelb, A. (1974). *Applied optimal estimation*. The M.I.T Press.
- Groves, P. D. (2013). *Principles of GNSS, inertial, and multisensor integrated navigation systems* (2nd ed.). Artech House.
- Heiskanen, W. A., & Moritz, H. (1967). Physical geodesy (book on physical geodesy covering potential theory, gravity fields, gravimetric and astrogeodetic methods, statistical analysis, etc).
- Huang, C., Li, A., Qin, F., Fang, J., & Chen, X. (2022). An atomic gravimeter dynamic measurement method based on Kalman filter. *Measurement Science and Technology*, 34, 015013.
- Jensen, T. E., Olesen, A. V., Forsberg, R., Olsson, P.-A., & Örijan, J. (2019). New results from strapdown airborne gravimetry using temperature stabilisation. *Remote Sensing*, 11(22), 2682. <https://doi.org/10.3390/rs11222682>
- Karcher, R., Imanaliev, A., Merlet, S., & Pereira dos Santos, F. (2018). Improving the accuracy of atom interferometers with ultracold sources. *New Journal of Physics*, 20(11), 113041. <https://doi.org/10.1088/1367-2630/aa07d>
- Kvas, A., Behzadpour, S., Ellmer, M., Klinger, B., Strasser, S., Zehentner, N., & Mayer-Gürr, T. (2019). ITSG-Grace2018: Overview and evaluation of a new grace-only gravity field time series. *Journal of Geophysical Research: Solid Earth*, 124(8), 9332–9344. <https://doi.org/10.1029/2019jb017415>
- Lan, S.-Y., Kuan, P.-C., Estey, B., Haslinger, P., & Müller, H. (2012). Influence of the coriolis force in atom interferometry. *Physical Review Letters*, 108(9), 090402. <https://doi.org/10.1103/physrevlett.108.090402>
- Lévêque, T., Antoni-Micollier, L., Faure, B., & Berthon, J. (2014). A laser setup for rubidium cooling dedicated to space applications. *Applied Physics B*, 116(4), 997–1004. <https://doi.org/10.1007/s00340-014-5788-z>
- Lévêque, T., Fallet, C., Manda, M., Biancale, R., Lemoine, J. M., Tardivel, S., et al. (2021). Gravity field mapping using laser-coupled quantum accelerometers in space. *Journal of Geodesy*, 95(1), 15. <https://doi.org/10.1007/s00190-020-01462-9>
- Ménoret, V., Vermeulen, P., Le Moigne, N., Bonvalot, S., Bouyer, P., Landragin, A., & Desruelle, B. (2018). Gravity measurements below 10- 9 g with a transportable absolute quantum gravimeter. *Scientific Reports*, 8(1), 12300. <https://doi.org/10.1038/s41598-018-30608-1>
- Metcalf, H. J., & Van der Straten, P. (2007). Laser cooling and trapping of neutral atoms. In *The optics encyclopedia: Basic foundations and practical applications*.
- Olesen, A. V. (2003). *Improved airborne scalar gravimetry for regional gravity field mapping and geoid determination (Unpublished doctoral dissertation)*. University of Copenhagen. Retrieved from [ftp.dsri.dk/pub/avo/AG/DOC/avo\[_\]techrep.pdf](ftp.dsri.dk/pub/avo/AG/DOC/avo[_]techrep.pdf)
- Pail, R., Bruinsma, S., Migliaccio, F., Förste, C., Goiginger, H., Schuh, W.-D., et al. (2011). First GOCE gravity field models derived by three different approaches. *Journal of Geodesy*, 85(11), 819–843. <https://doi.org/10.1007/s00190-011-0467-x>
- Pavlis, N. K., Holmes, S. A., Kenyon, S. C., & Factor, J. K. (2012). The development and evaluation of the Earth Gravitational Model 2008 (EGM2008). *Journal of Geophysical Research: Solid Earth*, 117(B4), B04406. <https://doi.org/10.1029/2011jb008916>
- Perrin, I., Bernard, J., Bidel, Y., Bonnin, A., Zahzam, N., Blanchard, C., et al. (2019). Zero-velocity atom interferometry using a retroreflected frequency-chirped laser. *Physical Review A*, 100(5), 053618. <https://doi.org/10.1103/physreva.100.053618>
- Reguzzoni, M., Migliaccio, F., & Batsukh, K. (2021). Gravity field recovery and error analysis for the MOCASS mission proposal based on cold atom interferometry. *Pure and Applied Geophysics*, 178(6), 2201–2222. <https://doi.org/10.1007/s00024-021-02756-5>
- Sánchez, L., Čunderlík, R., Dayoub, N., Mikula, K., Minarechová, Z., Šíma, Z., et al. (2016). A conventional value for the geoid reference potential w_0 . *Journal of Geodesy*, 90(9), 815–835. <https://doi.org/10.1007/s00190-016-0913-x>
- Sandwell, D. T., Müller, R. D., Smith, W. H., Garcia, E., & Francis, R. (2014). New global marine gravity model from CryoSat-2 and Jason-1 reveals buried tectonic structure. *Science*, 346(6205), 65–67. <https://doi.org/10.1126/science.1258213>
- Tamura, Y. (1987). A harmonic development of the tide-generating potential. *Marees Terrestres: Bulletin d'Informations*, 99, 6813–6855.
- Tino, G. M., & Kasevich, M. A. (2014). *Atom interferometry* (Vol. 188). IOS Press.
- Torge, W., & Müller, J. (2012). *Geodesy*. Walter de Gruyter.
- Tozer, B., Sandwell, D. T., Smith, W. H., Olson, C., Beale, J., & Wessel, P. (2019). Global bathymetry and topography at 15 arc sec: SRTM15+. *Earth and Space Science*, 6(10), 1847–1864. <https://doi.org/10.1029/2019ea000658>
- Trimeche, A., Battelier, B., Becker, D., Bertoldi, A., Bouyer, P., Braxmaier, C., et al. (2019). Concept study and preliminary design of a cold atom interferometer for space gravity gradiometry. *Classical and Quantum Gravity*, 36(21), 215004. <https://doi.org/10.1088/1361-6382/ab4548>
- Valliant, H. D. (1992). The Lacoste & Romberg air/sea gravity meter: An overview. In R. A. Geyer (Ed.), *CRC handbook of geophysical exploration at sea* (2nd ed., pp. 141–176).
- Zahzam, N., Christophe, B., Lebat, V., Hardy, E., Huynh, P., Marquet, N., et al. (2022). Hybrid electrostatic-atomic accelerometer for future space gravity missions. *Remote Sensing*, 14(14), 3273. <https://doi.org/10.3390/rs14143273>